2020-06-29

High Order Numerical Methods for Problems in Wave Scattering

Dane Scott Grundvig
Brigham Young University

BYU ScholarsArchive Citation

Grundvig, Dane Scott, "High Order Numerical Methods for Problems in Wave Scattering" (2020). *Theses and Dissertations*. 8617.
https://scholarsarchive.byu.edu/etd/8617

High Order Numerical Methods for Problems in Wave Scattering

Dane Scott Grundvig

A thesis submitted to the faculty of
Brigham Young University
in partial fulfillment of the requirements for the degree of

Master of Science

Vianey Villamizar, Chair
Emily Evans
Blake Barker

Department of Mathematics

Brigham Young University

ABSTRACT

High Order Numerical Methods for Problems in Wave Scattering

Dane Scott Grundvig
Department of Mathematics, BYU
Master of Science

Arbitrary high order numerical methods for time-harmonic acoustic scattering problems originally defined on unbounded domains are constructed. This is done by coupling recently developed high order local absorbing boundary conditions (ABCs) with finite difference methods for the Helmholtz equation. These ABCs are based on exact representations of the outgoing waves by means of farfield expansions. The finite difference methods, which are constructed from a deferred-correction (DC) technique, approximate the Helmholtz equation and the ABCs to any desired order. As a result, high order numerical methods with an overall order of convergence equal to the order of the DC schemes are obtained. A detailed construction of these DC finite difference schemes is presented. Details and results from an extension to heterogeneous media are also included. Additionally, a rigorous proof of the consistency of the DC schemes with the Helmholtz equation and the ABCs in polar coordinates is also given. The results of several numerical experiments corroborate the high order convergence of the proposed method. A novel local high order ABC for elastic waves based on farfield expansions is constructed and preliminary results applying it to elastic scattering problems are presented.

Keywords: acoustic scattering, elastic scattering, Helmholtz equation, high order numerical methods, variable wave number, heterogeneous media, deferred corrections

ACKNOWLEDGEMENTS

I will be forever indebted to Dr. Vianey Villamizar. Both for his help in the writing and research of this thesis as well as his willingness to take a chance on an inexperienced undergraduate math student. I also need to acknowledge the Brigham Young University ACME professors, they inspired my love of mathematics and were kind enough to also provide a solid mathematical foundation on which to build that love. Special thanks also goes to Otilio Rojas and Sebastian Acosta who contributed greatly to the work herein. Finally, thank you to my mother for being the first real mathematician in the family.

CONTENTS

LIST OF TABLES

LIST OF FIGURES

CHAPTER 1. INTRODUCTION

The propagation and scattering of waves in the presence of impenetrable obstacles, in an unbounded medium, is an important problem to which significant efforts have been dedicated. However, there are still aspects of this problem that have not yet been satisfactorily solved. One of them is the construction of easily implementable, reliable and stable high order numerical methods for the accurate approximation of scattered waves. This is the subject of this work. The construction of high order numerical methods is motivated by the need to obtain highly precise numerical solutions at relatively low computational costs. I consider scattering in two different media. The majority of my study is done for acoustic waves while I reserve the last part for the construction of a high order local absorbing boundary condition (ABC) for the elastic waves in unbounded domains.

Regarding acoustic media, it is well-known [1, 2, 3, 4] that the accuracy of the numerical methods for the Helmholtz equation (2.1) based on finite differences or finite elements deteriorates rapidly when the wave number k increases. This phenomenon is known as pollution error. A common practice, to avoid this error for a given numerical method, consists of increasing the number of points per wavelength $PPW = \lambda/h$, where λ is the wavelength and h represents the grid step size. However, this approach becomes computational very costly as k increases. An alternative to alleviate the computational cost is to employ high order numerical methods since they require less points per wavelength to achieve the same accuracy level as their low order counterparts. This is the approach followed in this work.

Among the most popular alternatives to finite difference methods are finite element (FEM) and boundary element methods (BEM). These methods have their own advantages and shortcomings when approximating the solutions of a boundary value problem (BVP). An important FEM advantage is their ability to deal with domains of arbitrary shape. However, high order convergence usually requires a high number of degrees of freedom which normally leads to elevated computational cost. The BEM have the advantage that the Sommerfeld radiation condition is already built into the numerical method, so there is no need to introduce an artificial boundary and define an ABC on it. In contrast, a major shortcoming of BEM is that they are limited to homogeneous media. In this study, I opt for finite difference methods because they are easy to use and their implementation is simple and flexible enough to be applied to heterogeneous media.

In the context of finite difference methods, there has been a lot of interest in high order numerical methods in recent years. In fact, for interior problems modeled by the Helmholtz equation, several fourth and sixth order numerical methods have appeared in the last 25 years. For instance, Singer and Turkel [5, 6] developed compact fourth and sixth order methods in two dimensions for constant wavenumber using Cartesian coordinates. Sutmann [7] devised a compact sixth order method for Dirichlet boundary value problems (BVPs) and Nabavi et al. [8] for Neumann BVPs. All of these compact numerical methods were obtained from the so called *equation-based* [5] procedure. By applying it, they obtained their compact fourth and sixth order 9-point finite difference formulas to approximate the two-dimensional Helmholtz equation in Cartesian coordinates. It resembles the strategy followed by Collatz and Leveque in [9, 10], respectively, to obtain the well-known compact 9-point finite difference formula for the two-dimensional Poisson equation in Cartesian coordinates. More recently, Zhang et al. [11] derived a sixth order finite difference scheme for the Helmholtz equation with inhomogeneous Robin boundary conditions in two dimensions.

A major challenge of the volumetric numerical methods, such as finite element and finite differences, when they are applied to wave scattering, is the need to transform a physical unbounded domain into a bounded one, such that the solution of the new bounded problem approximates to a reasonable degree the solution of the original unbounded problem in their common domain. This requires the introduction of both an artificial finite boundary and an appropriate ABC defined on this artificial boundary. One of the most important ABCs was introduced by Bayliss-Gunzburger-Turkel in their celebrated paper [12]. This condition is denoted as BGT in the ABC literature. Other well-known conditions in this category were introduced by Engquist-Majda [13], Feng [14] and Li-Cendes [15]. These conditions, in turn, have inspired others. The drawback of the BGT and the others mentioned is that to increase the order of the approximation at the boundary, the order of the derivatives present in their definitions also needs to be increased. This leads to impractical ABCs due to the difficulty found in their implementations beyond the first two orders. Many other ABCs have been formulated in recent years, for a complete review see the article by Givoli [16]. In this work, I adopt recently derived ABCs by Villamizar et al. [17]. These ABCs are based on finite truncations of exact series representations of the scattered field in the farfield region. They are also called *farfield expansions* ABCs. As a consequence, the order of the error induced by these ABCs can be easily improved by simply adding as many terms as needed to the truncated farfield expansions.

As far as the I know, overall high order finite difference methods for exterior time-harmonic acoustic scattering have only been constructed up to fourth order [18, 19, 20]. In the present study, I develop arbitrary high order finite difference schemes for the Helmholtz equation based on a *deferred-correction* (DC) methodology (see [10] Section 3.5). Among the pioneer applications of deferred-corrections to differential equations are the works by Pereyra [21, 22]. My construction proceeds by coupling arbitrary high order DC finite difference schemes for the Helmholtz equation with high order DC finite difference schemes corresponding to the arbitrary high order ABCs based on *farfield expansions*, which were developed by Villamizar et al. in [17]. As a result of combining these high order techniques (domain's interior and boundary), I obtain an overall arbitrary high order method for acoustic scattering. Of course, the arbitrary high order property of this method is limited by the computer arithmetic and the computer resources available. The construction and performance analysis of this overall and arbitrary high order finite difference method for acoustic scattering problems is discussed in detail in the following sections.

An important aspect of this work is the successful application of these higher order methods to wave scattering in heterogeneous media which is the content of Section 2.7. Also in Chapter 3, I construct a novel local high order ABC for elastic waves based on farfield expansions and present some preliminary results applying it to elastic scattering problems.

CHAPTER 2. HIGH ORDER NUMERICAL METHODS FOR ACOUSTIC SCATTERING

2.1 HIGH ORDER LOCAL ABSORBING BOUNDARY CONDITIONS (ABC)

When considering acoustic scattering, a classical strong formulation, when a time-harmonic incident wave, u_{inc}, is scattered from an obstacle with a boundary Γ embedded in an unbounded acoustic region Ω, consists of finding the acoustic scattered pressure field, $u \in C^2(\Omega) \cap C(\overline{\Omega})$ such that

$$\Delta u + k^2 u = f \qquad \text{in } \Omega, \tag{2.1}$$

$$u = -u_{\text{inc}} \qquad \text{or} \qquad \partial_n u = -\partial_n u_{\text{inc}}, \qquad \text{on } \Gamma, \tag{2.2}$$

$$\lim_{r\to\infty} r^{(\delta-1)/2} \left(\partial_r u - \mathrm{i} k u\right) = 0, \tag{2.3}$$

where Δ denotes the Laplace operator, ∂_n is the normal derivative and i is the imaginary unit. Both the wavenumber k and the source term f may vary in space. Here, I will consider the case where f has compact support in a bounded region $\Omega^- \subset \Omega$ that is bounded internally by Γ and externally by a circle of radius R. On Γ, I will study two boundary conditions at the scatterer, either the first equation in (2.2) corresponding to the sound-soft Dirichlet condition, or, the second equation in (2.2) corresponding to the sound-hard Neumann condition. Equation (2.3) is known as the Sommerfeld radiation condition, where $r = |\mathbf{x}|$ and $\delta = 2$ or 3 for two or three dimensions, respectively.

Definition 2.1. A solution u of the two-dimensional Helmholtz equation (2.1), exterior to a circle $r = R$ which also satisfies the Sommerfeld radiation condition (2.3) is called an *outgoing wave*.

All outgoing waves in 2D can be represented by two infinite series in powers of $1/kr$ whose representation is provided by the following theorem due to Karp.

Theorem 2.2. *[23] Let u be an outgoing solution of the two-dimensional Helmholtz equation in the exterior region to a circle $r = R$. Then u can be represented by a convergent expansion*

$$u(r,\theta) = H_0(kr)\sum_{l=0}^{\infty}\frac{F_l(\theta)}{(kr)^l} + H_1(kr)\sum_{l=0}^{\infty}\frac{G_l(\theta)}{(kr)^l}, \qquad r \geq R. \tag{2.4}$$

This series is uniformly and absolutely convergent for $r > R$ and can be differentiated term by term with respect to r and θ any number of times.

Here, r and θ are polar coordinates. The functions H_0 and H_1 are Hankel functions of the first kind of order 0 and 1, respectively. Karp also claimed that the terms F_l and G_l $(l = 1, 2, \dots)$ can be computed recursively from F_0 and G_0. To accomplish this, he suggested the substitution of the expansion (2.4) into Helmholtz equation in polar coordinates and the use of the identities: $H_0'(z) = -H_1(z)$ and $H_1' = H_0(z) - \frac{1}{z}H_1(z)$. In fact, by doing this and requiring the coefficients of H_0 and H_1 to vanish, a recurrence formula for the coefficients F_l and G_l for the expansion (2.4) can be derived. This result is stated in the following corollary.

Corollary 2.3. *The coefficients $F_l(\theta)$ and $G_l(\theta)$ $(l > 1)$ of the expansion (2.4), can be determined from $F_0(\theta)$ and $G_0(\theta)$ by the recursion formulas*

$$\begin{aligned} 2lG_l(\theta) &= (l-1)^2F_{l-1}(\theta) + d_\theta^2 F_{l-1}(\theta), && \textit{for } l = 1, 2, \dots \\ 2lF_l(\theta) &= -l^2G_{l-1}(\theta) - d_\theta^2 G_{l-1}(\theta), && \textit{for } l = 1, 2, \dots. \end{aligned}$$

These formulas have led to the derivation of several high order local ABCs for time-harmonic acoustic scattering. Of particular note is the work of Bayliss-Gunzburger-Turkel [12] in developing their well-known BGT absorbing boundary condition. In their pioneering work, they began by developing an asymptotic expansion of (2.4) given by,

$$u \approx \frac{e^{ikr}}{\sqrt{kr}}\sum_{l=0}^{\infty}\frac{f_l(\theta)}{r^l}, \qquad \text{as } r \to \infty, \tag{2.5}$$

with recursion formula

$$2ilf_l(\theta) = (l - \frac{1}{2})^2 f_{l-1}(\theta) + \partial_\theta^2 f_{l-1}(\theta), \qquad l \geq 1.$$

These equations can then be used to construct a sequence of local ABCs using a technique called operator annihilation. The first of these local absorbing boundary conditions (ABCs) are defined by the following differential operators:

$$\begin{aligned}
&\mathcal{B}_0 u = \partial_r u - iku \in \mathcal{O}\left(\frac{1}{r^{3/2}}\right),\\
&\mathcal{B}_1 u = \partial_r u - iku + \frac{u}{2r} \in \mathcal{O}\left(\frac{1}{r^{5/2}}\right),\\
&\mathcal{B}_2 u = \partial_r^2 u + \left(\frac{3}{r} - 2ik\right)\partial_r u + \left(\frac{3}{4r} - 3ik\right)\frac{u}{r} - k^2 u \in \mathcal{O}\left(\frac{1}{r^{9/2}}\right).
\end{aligned}$$

Although these ABCs are useful, there are some problems when using the higher order versions. In fact, in order to use higher order versions, the number of terms required and the order of the derivatives both increase with respect to the order. As a consequence, the ABCs constructed from the operators $\mathcal{B}_i$ for $i > 2$ are numerically intractable.

After the appearance of this pioneer BGT absorbing boundary condition, many more followed. Most of these ABCs were based on the same annihilating technique. To the best of my knowledge, there are only two local high order ABC, that are numerically tractable, one of them is due to Hagstrom and Hariharan [24]. Unfortunatley, this ABC is based on the series representation (2.5) of the scattered field, which is only an asymptotic approximation to Karp's exact representation. The other one is due to Villamizar et al. [17] who use Karp's expansion directly to define a more precise and computational more efficient local ABC. This is the one that I will use in this work. The details of its definition and implementation are considered in the next section.

2.2 FORMULATION OF THE ACOUSTIC SCATTERING BVP WITH KARP'S FARFIELD EXPANSION ABC

Instead of formulating an ABC using the BGT condition, Villamizar et al. [17] used a more direct application of Karp's exact expansion (2.4). This was done by first introducing a circular artificial boundary S that encloses all scatterers, regardless of their particular shapes, and then by defining high order local ABCs on the artificial boundary S. Note that the artificial boundary S divides the domain into a bounded computational region Ω^- enclosed by the obstacle boundary Γ and the artificial boundary S, and the exterior unbounded region $\Omega^+ = \Omega \backslash \bar{\Omega}^-$. Once this decomposition of the domain is done, the original unbounded problem in Ω is reformulated as a bounded problem in Ω^- by matching the solution u inside Ω^- with the karp's semi-analytical series representation (2.4) of the solution u in Ω^+.

With the given parameters, a complete boundary value problem can be formulated using the following equations:

$$\Delta u + k^2 u = 0, \qquad \text{in} \quad \Omega^-, \tag{2.6}$$

$$u = -u_{\text{inc}}, \qquad \text{or} \qquad \partial_r u = -\partial_r u_{\text{inc}}, \qquad \text{in} \quad \Gamma, \tag{2.7}$$

$$u(R,\theta) = H_0(kR) \sum_{l=0}^{L-1} \frac{F_l(\theta)}{(kR)^l} + H_1(kR) \sum_{l=0}^{L-1} \frac{G_l(\theta)}{(kR)^l}, \tag{2.8}$$

$$\partial_r u(R,\theta) = \partial_r \left(H_0(kr) \sum_{l=0}^{L-1} \frac{F_l(\theta)}{(kr)^l} + H_1(kr) \sum_{l=0}^{L-1} \frac{G_l(\theta)}{(kr)^l} \right) \Bigg|_{r=R}, \tag{2.9}$$

$$\partial_r^2 u(R,\theta) = \partial_r^2 \left(H_0(kr) \sum_{l=0}^{L-1} \frac{F_l(\theta)}{(kr)^l} + H_1(kr) \sum_{l=0}^{L-1} \frac{G_l(\theta)}{(kr)^l} \right) \Bigg|_{r=R}, \tag{2.10}$$

$$2lG_l(\theta) = (l-1)^2 F_{l-1}(\theta) + d_\theta^2 F_{l-1}(\theta), \qquad \text{for } l = 1, 2, \ldots \tag{2.11}$$

$$2lF_l(\theta) = -l^2 G_{l-1}(\theta) - d_\theta^2 G_{l-1}(\theta), \qquad \text{for } l = 1, 2, \ldots, \tag{2.12}$$

where R is the radius of the circular artificial boundary S. Equations (2.6)-(2.7) guarantee that u is an outgoing wave, however, with only those equations, there are not enough independent equations to solve for the number of unknowns. To that end, two additional conditions, (2.8) and (2.9) which match the first and second derivatives of the interior outgoing wave with the Karp expansion at the boundary R, are added. These equations allow for the computation of the unknown functions F_0 and G_0. To complete the problem, additional conditions in the form of equations (2.11) and (2.12) are added. These equations come from Corollary 2.3 and allow F_l and G_l for $l = 1, \ldots, L-1$ to be computed. Thus, the equations (2.8)-(2.12) constitute the novel *Karp's farfield expansion* ABC (KFE) constructed in [17].

As a note, I chose to limit my study to the two-dimensional Helmholtz equation in polar coordinates for clarity in the formulation and presentation of the theoretical results. However, I anticipate that an extension of the DC technique to the KFE-BVP in generalized curvilinear coordinates will follow a similar pattern to that found in polar coordinates. I discuss this extension in the concluding remarks in Section 4.

2.3 DERIVATION OF HIGH ORDER DEFERRED-CORRECTION (DC) NUMERICAL METHODS

In the next subsections, the detailed formulation of the fourth order DC numerical scheme is given for the Helmholtz equation in the domain Ω^- bounded externally by the artificial boundary S of circular shape with radius R. Similarly, I also develop the fourth order DC scheme for the construction of the high order KFE imposed on the artificial boundary. Then I proceed to go over the extension to arbitrary high order DC schemes.

2.3.1 Fourth order DC scheme for the Helmholtz equation in polar coordinates. First, I consider that the domain Ω^- can be covered by a polar grid with constant radial and angular steps Δr and $\Delta\theta$, respectively. The number of grid points in the radial and angular directions is $N, m > 1$, respectively. For a given grid point (r_i, θ_j), the discrete value of the scattered field is denoted by $u_{i,j} = u(r_i, \theta_j)$. Notice that the pairs (r_i, θ_1) and (r_i, θ_{m+1}) represent the same physical point due to periodicity in the angular direction, thus $u_{i,1} = u_{i,m+1}$ for $i \leq N$. Thus, the grid supports $N \times m$ wavefield evaluations.

I start with the standard centered second order finite difference method for the Helmholtz equation in polar coordinates given by

$$\begin{aligned}\mathcal{H}^2 U^2_{ij} \equiv \frac{U^2_{i+1,j} - 2U^2_{i,j} + U^2_{i-1,j}}{\Delta r^2} + \frac{1}{r_i}\frac{U^2_{i+1,j} - U^2_{i-1,j}}{2\Delta r} \\ + \frac{1}{r_i^2}\frac{U^2_{i,j+1} - 2U^2_{i,j} + U^2_{i,j-1}}{\Delta\theta^2} + k^2 U^2_{ij} = 0.\end{aligned} \tag{2.13}$$

The symbol U^2_{ij} is used to describe a discrete solution of (2.13). The super-index 2 states that $\mathcal{H}^2 U^2_{ij} = 0$ is a consistent second order finite difference approximation of the Helmholtz equation (2.6). Also, I consider a discrete function U^2_{ij} which is a second order approximation to the exact solution u of the Helmholtz equation (2.6) subject to the boundary conditions (2.7)-(2.12), i.e.,

$$U^2_{ij} = u(r_i,\theta_j) + \Delta r^2 v(r_i,\theta_j) + \Delta\theta^2 w(r_i,\theta_j) = u(r_i,\theta_j) + h^2 z(r_i,\theta_j), \tag{2.14}$$

where v, and w and z are sufficiently smooth bounded functions on the closure of Ω^- and $h = \max\{\Delta r, \Delta\theta\}$. The computation of U^2_{ij} is fully described in [17].

Applying $\mathcal{H}^2$ to u and evaluating it at (r_i,θ_j) leads to

$$\begin{aligned}\mathcal{H}^2 u_{ij} &= \frac{u_{i+1,j} - 2u_{i,j} + u_{i-1,j}}{\Delta r^2} + \frac{1}{r_i}\frac{u_{i+1,j} - u_{i-1,j}}{2\,\Delta r} + \frac{1}{r^2}\frac{u_{i,j+1} - 2u_{i,j} + u_{i,j-1}}{\Delta\theta^2} + k^2 u_{ij} \\ &= \left(\Delta_{r\theta} u + k^2 u\right)_{ij} + \frac{\Delta r^2}{12}\left((u_{4r})_{ij} + \frac{2}{r_i}(u_{3r})_{ij}\right) + \frac{\Delta\theta^2}{12\,r_i^2}(u_{4\theta})_{ij} + O(\Delta r^4) + O(\Delta\theta^4).\end{aligned} \tag{2.15}$$

I seek to obtain a fourth order finite difference scheme for the Helmholtz equation by subtracting the second order leading terms of the truncation error in the right hand side of (2.15) from the second order standard scheme (2.13). This is followed by substitution of the partial derivatives of u, present in these leading terms, by finite difference operators approximating these partial derivatives of u to second order. They act on the previously computed discrete solution U^2_{ij} of the standard second order scheme (2.13) which approximates u to second order. This is the fundamental idea in the formulation of the DC method proposed in this work for the Helmholtz equation. More precisely, the construction of the fourth order DC technique for the Helmholtz equation (2.6) subject to the boundary conditions (2.7)-(2.12) consists of two steps:

Step 1: *Obtaining a second order approximation U^2_{ij} to the solution u, of the original BVP (2.1)-(2.3).*

Approximate the Helmholtz equation (2.6) by the standard centered second order 5-point stencil scheme $\mathcal{H}^2 U^2_{ij} = 0$, defined in (2.13). Also, use appropriate one-sided second order schemes to approximate all the other boundary differential operators contained in the boundary conditions (2.7)-(2.12). Then, by solving the linear system that ultimately results from the discretization of all the equations of the KFE-BVP, obtain a second order numerical approximation U^2_{ij} to the exact solution u, of the original BVP (see [17] for details).

Step 2: *Formulation of the new fourth order finite difference DC numerical scheme for the Helmholtz equation in terms of the U^2_{ij} obtained in step 1.*

The second step consists of approximating the continuous derivatives u_{4r}, u_{3r}, and $u_{4\theta}$ in (2.15) using standard centered second order finite differences acting on U^2_{ij} as follows,

$$(u_{4r})_{ij} \approx D^2_{4r} U^2_{ij} \equiv \frac{1}{\Delta r^4}\left[U^2_{i-2,j} - 4U^2_{i-1,j} + 6U^2_{i,j} - 4U^2_{i+1,j} + U^2_{i+2,j}\right], \tag{2.16}$$

$$(u_{3r})_{ij} \approx D^2_{3r} U^2_{ij} \equiv \frac{1}{\Delta r^3}\left[-\frac{1}{2}U^2_{i-2,j} + U^2_{i-1,j} - U^2_{i+1,j} + \frac{1}{2}U^2_{i+2,j}\right], \tag{2.17}$$

$$(u_{4\theta})_{ij} \approx D^2_{4\theta} U^2_{ij} \equiv \frac{1}{\Delta \theta^4}\left[U^2_{i,j-2} - 4U^2_{i,j-1} + 6U^2_{i,j} - 4U^2_{i,j+1} + U^2_{i,j+2}\right]. \tag{2.18}$$

I use the notation D^p_{qr} to designate the pth order centered finite difference discrete operator of the qth derivative with respect to r. Analogously, $D^p_{q\theta}$ designates the pth order centered finite difference operator of the qth order derivative with respect to θ. Then by substituting (2.16)-(2.18) into (2.15), I arrive to the new fourth order finite difference DC numerical scheme for the Helmholtz equation given by

$$\begin{aligned}\mathcal{H}^4 U^4_{ij} \equiv \frac{U^4_{i+1,j} - 2U^4_{i,j} + U^4_{i-1,j}}{\Delta r^2} + \frac{1}{r_i}\frac{U^4_{i+1,j} - U^4_{i-1,j}}{2\Delta r} + \frac{1}{r_i^2}\frac{U^4_{i,j+1} - 2U^4_{i,j} + U^4_{i,j-1}}{\Delta\theta^2} + k^2 U^4_{ij} \\ - \frac{\Delta r^2}{12}\left(D^2_{4r}U^2_{ij} + \frac{2}{r_i}D^2_{3r}U^2_{ij}\right) - \frac{\Delta\theta^2}{12 r_i^2} D^2_{4\theta}U^2_{ij} = 0.\end{aligned} \tag{2.19}$$

Notice that the new finite difference scheme (2.19) for the unknown discrete function U^4_{ij} consists of the same 5-point stencil of the standard centered second order scheme. The difference is that (2.19) has additional known terms given by

$$\frac{\Delta r^2}{12}\left(D^2_{4r}U^2_{ij} + \frac{2}{r_i}D^2_{3r}U^2_{ij}\right) + \frac{\Delta\theta^2}{12 r_i^2} D^2_{4\theta}U^2_{ij},$$

which are calculated from the second order numerical solution U^2_{ij} of u already computed in the first step.

Remark 1. At the artificial boundary $r = R$, I use appropriate second order one-sided finite differences acting on U^2_{Nj} to approximate the various derivatives present in the leading terms of the truncation error in (2.15). They are defined in the following section.

In what follows, I state and prove my claim that the finite difference scheme (2.19) is a fourth order approximation of the Helmholtz equation.

Theorem 2.4. *The new DC numerical scheme (2.19), or equivalently,*

$$\mathcal{H}^4 {U^4}_{ij} \equiv \mathcal{H}^2 U^4_{ij} - \frac{\Delta r^2}{12}\left(D^2_{4r}U^2_{ij} + \frac{2}{r_i}D^2_{3r}U^2_{ij}\right) - \frac{\Delta\theta^2}{12 r_i^2} D^2_{4\theta}U^2_{ij} = 0 \tag{2.20}$$

is a consistent finite difference approximation of the Helmholtz equation in polar coordinates,

$$\Delta_{r\theta}u + k^2 u = u_{rr} + \frac{1}{r}u_r + \frac{1}{r^2}u_{\theta\theta} + k^2 u = 0$$

of order $\mathcal{O}(\Delta r^4) + \mathcal{O}(\Delta\theta^4) + \mathcal{O}(\Delta r^2 \Delta\theta^2)$*, if the continuous function* u *has derivatives of order 4 in its two variables* r *and* θ*; and if the discrete function* U^2_{ij} *is a second order approximation of* u*, i.e., there exists* $v(r,\theta)$*, and* $w(r,\theta)$ *sufficiently smooth and bounded functions on the closure of* Ω^- *such that*

$$U^2_{ij} = u(r_i, \theta_j) + \Delta r^2 v(r_i, \theta_j) + \Delta\theta^2 w(r_i, \theta_j) = u_{ij} + \Delta r^2 v_{ij} + \Delta\theta^2 w_{ij}. \tag{2.21}$$

Before proving this theorem, I will prove the following lemma.

Lemma 2.5. *For* U^2_{ij} *and* $u(r,\theta)$ *satisfying the hypotheses of Theorem 2.4, it holds that the standard second order centered finite difference operators:*

(i) D^2_{4r}*, as defined in (2.16), acting on* U^2_{ij}*, is consistent with the derivative* u_{4r} *of order* $\mathcal{O}(\Delta r^2)+$ $O(\Delta\theta^2)$.

(ii) D^2_{3r}*, as defined in (2.17), acting on* U^2_{ij}*, is consistent with the derivative* u_{3r} *of order* $\mathcal{O}(\Delta r^2)+$ $\mathcal{O}(\Delta\theta^2)$

(iii) $D^2_{4\theta}$*, as defined in (2.18), acting on* U^2_{ij}*, is consistent with the derivative* $u_{4\theta}$ *of order* $\mathcal{O}(\Delta\theta^2)+$ $\mathcal{O}(\Delta r^2)$

Proof. To prove (a), I apply D^2_{4r} to U^2_{ij} replaced by (2.21). This leads to

$$\begin{aligned} D^2_{4r} U^2_{ij} &= D^2_{4r} u_{ij} + \Delta r^2 D^2_{4r} v_{ij} + \Delta\theta^2 D^2_{4r} w_{ij} \\ &= (u_{4r})_{ij} + \mathcal{O}(\Delta r^2) + \Delta r^2 (v_{4r})_{ij} + \mathcal{O}(\Delta r^4) + \Delta\theta^2 (w_{4r})_{ij} + \mathcal{O}(\Delta\theta^2 \Delta r^2) \end{aligned}$$

Therefore,

$$D^2_{4r} U^2_{ij} = (u_{4r})_{ij} + \mathcal{O}(\Delta r^2) + \mathcal{O}(\Delta\theta^2)$$

and part (a) of the lemma is proved. The proofs of parts (b) and (c) are completely analogous. $\square$

Proof. (Proof of Theorem 2.4)

First, I rewrite $\mathcal{H}^4 U^4_{ij}$ as

$$\mathcal{H}^4 U^4_{ij} = \left(D^2_{2r} U^4_{ij} - \frac{\Delta r^2}{12} D^2_{4r} U^2_{ij} \right) + \frac{1}{r_i} \left(D^2_{r} U^4_{ij} - \frac{\Delta r^2}{6} D^2_{3r} U^2_{ij} \right)$$
$$+ \frac{1}{r_i^2} \left(D^2_{2\theta} U^4_{ij} - \frac{\Delta \theta^2}{12} D^2_{4\theta} U^2_{ij} \right) + k^2 \bar{U}_{ij}.$$

Next, I apply $\mathcal{H}^4$ to u satisfying (2.21). This is followed by expressing each of the discrete derivatives of u in terms of their corresponding continuous derivatives plus their leading order truncation errors, which leads to

$$\mathcal{H}^4 u_{ij} = \left((u_{rr})_{ij} + \frac{\Delta r^2}{12} (u_{4r})_{ij} + \mathcal{O}(\Delta r^4) - \frac{\Delta r^2}{12} D^2_{4r} U^2_{ij} \right)$$
$$+ \frac{1}{r_i} \left((u_{r})_{ij} + \frac{\Delta r^2}{6} (u_{3r})_{ij} + \mathcal{O}(\Delta r^4) - \frac{\Delta r^2}{6} D^2_{3r} U^2_{ij} \right)$$
$$+ \frac{1}{r_i^2} \left((u_{\theta\theta})_{ij} + \frac{\Delta \theta^2}{12} (u_{4\theta})_{ij} + \mathcal{O}(\Delta \theta^4) - \frac{\Delta \theta^2}{12} D^2_{4\theta} U^2_{ij} \right) + k^2 u_{ij}.$$

Reordering the righthand side terms yields

$$\mathcal{H}^4 u_{ij} = (u_{rr})_{ij} + \frac{1}{r_i} (u_r)_{ij} + \frac{1}{r_i^2} (u_{\theta\theta})_{ij} + k^2 u_{ij} - \frac{\Delta r^2}{12} \left(D^2_{4r} U^2_{ij} - (u_{4r})_{ij} \right)$$
$$- \frac{\Delta r^2}{6} \left(D^2_{3r} U^2_{ij} - (u_{3r})_{ij} \right) - \frac{\Delta \theta^2}{12} \left(D^2_{4\theta} U^2_{ij} - (u_{4\theta})_{ij} \right) + \mathcal{O}(\Delta r^4) + \mathcal{O}(\Delta \theta^4).$$

Then, by applying the statements of Lemma 2.5 to the above expression, I get

$$\mathcal{H}^4 u_{ij} = \left(\Delta_{r\theta} u + k^2 u \right)_{ij} + \mathcal{O}(\Delta r^4) + \mathcal{O}(\Delta \theta^4) + \mathcal{O}(\Delta r^2 \Delta \theta^2),$$

which finishes the proof. □

Therefore, the new numerical scheme (2.19) approximates the Helmholtz equation to fourth order, while maintaining a 5-point stencil on the unknown discrete function U^4_{ij}. This leads to a significant improvement on precision with respect to the 5-point standard second order finite difference at the same computational cost. Furthermore, there are important savings in the required storage and computational time compared to the 9-point standard centered fourth order finite difference approximation of the Helmholtz equation, as shown by my results in Section 2.6. This is the main virtue of the DC technique developed in this work.

2.3.2 Fourth order DC approximation at the artificial boundary. At the absorbing boundary, the radial derivatives of the scattered field u, present in (2.9) and (2.10), are approximated using standard centered second order finite differences. Then, to increase their accuracy to fourth order via DC, I subtract from these standard finite differences their leading order truncation error terms. Imitating the previous procedure employed for the Helmholtz equation at the interior points, these leading order terms are approximated using a previously calculated second order numerical solution U^2_{ij} of the exact solution u of the BVP (2.6)-(2.12). As a result, I obtain the following discrete non-homogeneous equations at the artificial boundary $r = R$:

$$\frac{U^4_{N+1,j} - U^4_{N-1,j}}{2\Delta r} - \left.\partial_r\left(H_0(kr)\sum_{l=0}^{L-1}\frac{F^4_{lj}}{r^l} + H_1(kr)\sum_{l=0}^{L-1}\frac{G^4_{lj}}{r^l}\right)\right|_{r=r_N=R} = \frac{\Delta r^2}{6}(Dl)^2_{3r}U^2_{N,j} \quad (2.22)$$

$$\frac{U^4_{N+1,j} - 2U^4_{Nj} + U^4_{N-1,j}}{\Delta r^2} - \left.\partial^2_r\left(H_0(kr)\sum_{l=0}^{L-1}\frac{F^4_{lj}}{r^l} + H_1(kr)\sum_{l=0}^{L-1}\frac{G^4_{lj}}{r^l}\right)\right|_{r=r_N=R} = \frac{\Delta r^2}{12}(Dl)^2_{4r}U^2_{N,j}. \quad (2.23)$$

The forcing terms in (2.22) and (2.23) are defined from one-sided second order finite difference approximations $(Dl)^2_{3r}U^2_{N,j}$ and $(Dl)^2_{4r}U^2_{N,j}$ of $(u_{3r})_{Nj}$ and $(u_{4r})_{Nj}$, respectively. More precisely,

$$(Dl)^2_{3r}U^2_{N,j} \equiv \frac{1}{\Delta r^3}\left[\frac{1}{2}U^2_{N-3,j} - 3U^2_{N-2,j} + 6U^2_{N-1,j} - 5U^2_{N,j} + \frac{3}{2}U^2_{N+1,j}\right] \quad (2.24)$$

$$(Dl)^2_{4r}U^2_{N,j} \equiv \frac{1}{\Delta r^4}\left[-U^2_{N-4,j} + 6U^2_{N-3,j} - 14U^2_{N-2,j} + 16U^2_{N-1,j} - 9U^2_{N,j} + 2U^2_{N+1,j}\right]. \quad (2.25)$$

Notice that the equations (2.22)- (2.23) involve values of the discrete approximations, U^4_{ij} and U^2_{ij}, at the ghost points (r_{N+1}, θ_j). The unknowns $U^4_{N+1,j}$ also appear in the fourth order approximation of the Helmholtz equation (2.19) evaluated at $i = N$ for $j = 1 \ldots m$. I eliminate it by solving for

$U^4_{N+1,j}$ in (2.22) and substituting it into (2.23), and into (2.19) evaluated at $i = N$. Similarly, the ghost values $U^2_{N+1,j}$ are computed during the first step, i.e., as part of the numerical solution of the second order scheme of the KFE-BVP (2.6)-(2.12).

Analogously, I construct deferred-correction fourth order recursion formulas by keeping the second order terms of the truncation errors obtained by approximating the angular derivatives in (2.11)-(2.12) using second order centered finite differences. In fact,

$$2lG^4_{lj} - (l-1)^2 F^4_{l-1,j} - \frac{F^4_{l-1,j+1} - 2F^4_{l-1,j} + F^4_{l-1,j-1}}{\Delta\theta^2} = -\frac{\Delta\theta^2}{12} D^2_{4\theta} F^2_{l-1,j}, \tag{2.26}$$

$$2lF^4_{lj} + l^2 G^4_{l-1,j} + \frac{G^4_{l-1,j+1} - 2G^4_{l-1,j} + G^4_{l-1,j-1}}{\Delta\theta^2} = \frac{\Delta\theta^2}{12} D^2_{4\theta} G^2_{l-1,j}, \tag{2.27}$$

where $F^2_{l-1,j}$ and $G^2_{l-1,j}$, obtained in the first step, are second order approximations of $F_{l-1,j}$ and $G_{l-1,j}$ which are part of the exact solution of the original scattering BVP. Also, the discrete differential operator $D^2_{4\theta}$ is defined by equation (2.18) of the previous section.

Remark 2. The proofs that the finite difference formulas (2.22)-(2.23) and (2.26)-(2.27) approximate their continuous counterparts to fourth order are very similar to the proof of Theorem 2.4. Therefore, they are omitted. The key assumption for these proof is that the discrete functions $U^2_{N,j}$, $F^2_{l-1,j}$ and $G^2_{l-1,j}$, which are obtained in step 1, are second order approximations of $u(R,\theta)$, $F_{l-1}(\theta)$, and $G_{l-1}(\theta)$, respectively.

Summarizing, the set of algebraic equations (2.19), (2.22)-(2.23), (2.26)-(2.27), the discrete versions of the continuity of the scattered field (2.8) and the boundary condition at the obstacle (2.7) form the fourth order Karp DC system of linear equations to be solved. I denote this system as *KDC4*. Details on the structure and solution of this linear system are given in Section 2.5.

2.3.3 General high order DC schemes for the Helmholtz equation in polar coordinates.

In this Section, I extend the derivation of of the fourth order DC scheme for the BVP (2.6)-(2.12) modeled by the Helmholtz equation in Subsections 2.3.1-2.3.2 to a scheme of arbitrary high order. To start this derivation, I assume that $U^{(p-2)}_{ij}$ is a $(p-2)$th order discrete approximation of the solution u of the Helmholtz equation (2.6) subject to the boundary conditions (2.7)-(2.12). The details on the computation of this discrete approximation will be discussed later. Then, I apply the standard centered second order finite difference approximation $\mathcal{H}^2$ of the Helmholtz operator to the solution u and retain up to the $(p-2)$ leading order terms of the truncation errors of each Helmholtz derivative. As a result, I obtain

$$
\begin{aligned}
\mathcal{H}^2 u_{ij} = \frac{u_{i+1,j} - 2u_{ij} + u_{i-1,j}}{h^2} &+ \frac{1}{r_i}\frac{u_{i+1,j} - u_{i-1,j}}{2\,h} + \frac{1}{r^2}\frac{u_{i,j+1} - 2u_{ij} + u_{i,j-1}}{h^2} + k^2 u_{ij} = \\
&- \left(\frac{1}{3!r_i}(u_{3r})_{ij} + \frac{2}{4!}(u_{4r})_{ij} + \frac{2}{4!r_i^2}(u_{4\theta})_{ij}\right) h^2 \\
&- \left(\frac{1}{5!r_i}(u_{5r})_{ij} + \frac{2}{6!}(u_{6r})_{ij} + \frac{2}{6!r_i^2}(u_{6\theta})_{ij}\right) h^4 \dots \\
&- \left(\frac{1}{(p-1)!r_i}(u_{(p-1)r})_{ij} + \frac{2}{p!}(u_{pr})_{ij} + \frac{2}{p!r_i^2}(u_{p\theta})_{ij}\right) h^{p-2} + \mathcal{O}(h^p),
\end{aligned}
\tag{2.28}
$$

where $p = 4, 6, \dots$, and $h \equiv \max\{\Delta r, \Delta\theta\}$.

I continue the construction of the pth order DC approximation to the Helmholtz equation by imitating the one used to obtain the 4th order DC approximation (2.19). In fact, I proceed by subtracting all of up to $(p-2)$th order error terms from the middle member of the equation (2.28). This is followed by substituting the continuous derivatives present in these error terms, by appropriate finite difference approximations of them acting on the $(p-2)$th order discrete approximation, U_{ij}^{p-2}, of the exact solution u. More precisely, for $q = 4, 6, 8, \dots, p$, I replace the continuous derivatives of the exact solution $(u_{qr})_{ij}$, $\left(u_{(q-1)r}\right)_{ij}$, and $(u_{q\theta})_{ij}$ in (2.28) by a $(p+2-q)$th order finite difference approximations given by $D_{qr}^{p+2-q}U_{ij}^{p-2}$, $D_{(q-1)r}^{p+2-q}U_{ij}^{p-2}$, and $D_{q\theta}^{p+2-q}U_{ij}^{p-2}$, respectively. This construction suggests the definition of the following pth order DC finite difference approximation to the Helmholtz differential operator,

$$
\begin{aligned}
\mathcal{H}^p U_{ij}^p \equiv\ & \frac{U_{i+1,j}^p - 2U_{ij}^p + U_{i-1,j}^p}{h^2} + \frac{1}{r_i}\frac{U_{i+1,j}^p - U_{i-1,j}^p}{2\,h} + \frac{1}{r^2}\frac{U_{i,j+1}^p - 2U_{ij}^p + U_{i,j-1}^p}{h^2} + k^2 U_{ij}^p \\
& - \left(\frac{1}{3!r_i} D_{3r}^{p-2} U_{ij}^{p-2} + \frac{2}{4!} D_{4r}^{p-2} U_{ij}^{p-2} + \frac{2}{4!r_i^2} D_{4\theta}^{p-2} U_{ij}^{p-2}\right) h^2 \\
& - \left(\frac{1}{5!r_i} D_{5r}^{p-4} U_{ij}^{p-2} + \frac{2}{6!} D_{6r}^{p-4} U_{ij}^{p-2} + \frac{2}{6!r_i^2} D_{6\theta}^{p-4} U_{ij}^{p-2}\right) h^4 - \dots \\
& - \left(\frac{1}{(p-1)!r_i} D_{(p-1)r}^{2} U_{ij}^{p-2} + \frac{2}{p!} D_{pr}^{2} U_{ij}^{p-2} + \frac{2}{p!r_i^2} D_{p\theta}^{2} U_{ij}^{p-2}\right) h^{p-2}.
\end{aligned}
\tag{2.29}
$$

I claim that the equation, $\mathcal{H}^p U_{ij}^p = 0$, is consistent with the Helmholtz equation (2.6) of order $\mathcal{O}(h^p)$. This is the content of my next theorem whose proof is provided below. The formulas for the discrete differential operators acting on U_{ij}^{p-2}, i.e., $D_{qr}^{p+2-q} U_{ij}^{p-2}$, $D_{(q-1)r}^{p+2-q} U_{ij}^{p-2}$, and $D_{q\theta}^{p+2-q} U_{ij}^{p-2}$ for arbitrary p and $q = 4, \dots p$, can be obtained by applying computational algorithms such as *fdcoeffF.m* written as a MATLAB function by Leveque [10]. As an illustrative example, I define the operators needed to obtain a sixth order DC scheme, $p = 6$ and $q = 4, 6$ in the Appendix A.

Notice that the new finite difference operator $\mathcal{H}^p$ in (2.29) acts on the unknown discrete function U_{ij}^p, generating the same 5-point stencil of the standard centered second order discrete operator $\mathcal{H}^2$. The difference is in the additional known terms which depend on the numerical approximation U_{ij}^{p-2} of the exact solution u. They are given by

$$
\begin{aligned}
& \left(\frac{1}{3!r_i} D_{3r}^{p-2} U_{ij}^{p-2} + \frac{2}{4!} D_{4r}^{p-2} U_{ij}^{p-2} + \frac{2}{4!r_i^2} D_{4\theta}^{p-2} U_{ij}^{p-2}\right) h^2 + \dots \\
& \qquad + \left(\frac{1}{(p-1)!r_i} D_{(p-1)r}^{2} U_{ij}^{p-2} + \frac{2}{p!} D_{pr}^{2} U_{ij}^{p-2} + \frac{2}{p!r_i^2} D_{p\theta}^{2} U_{ij}^{p-2}\right) h^{p-2}.
\end{aligned}
$$

Remark 3. Near the artificial boundary $r = R$, I use appropriate one-sided finite difference to approximate the various derivatives present in the leading terms of the truncation error in (2.29).

Theorem 2.6. *The new DC numerical scheme,*

$$\begin{aligned}\mathcal{H}^p U_{ij}^p \equiv \mathcal{H}^2 U_{ij}^p &- \left(\frac{1}{3!r_i} D_{3r}^{p-2} U_{ij}^{p-2} + \frac{2}{4!} D_{4r}^{p-2} U_{ij}^{p-2} + \frac{2}{4!r_i^2} D_{4\theta}^{p-2} U_{ij}^{p-2}\right) h^2 \\ &- \left(\frac{1}{5!r_i} D_{5r}^{p-4} U_{ij}^{p-2} + \frac{2}{6!} D_{6r}^{p-4} U_{ij}^{p-2} + \frac{2}{6!r_i^2} D_{6\theta}^{p-4} U_{ij}^{p-2}\right) h^4 - \dots \\ &- \left(\frac{1}{(p-1)!r_i} D_{(p-1)r}^{2} U_{ij}^{p-2} + \frac{2}{p!} D_{pr}^{2} U_{ij}^{p-2} + \frac{2}{p!r_i^2} D_{p\theta}^{2} U_{ij}^{p-2}\right) h^{p-2} = 0, \quad (2.30)\end{aligned}$$

is a consistent finite difference approximation of the Helmholtz equation in polar coordinates

$$\Delta_{r\theta} u + k^2 u = u_{rr} + \frac{1}{r} u_r + \frac{1}{r^2} u_{\theta\theta} + k^2 u = 0$$

of order $\mathcal{O}(h^p)$, if the continuous function u has derivatives of order p in its two variables r and θ; and if the discrete function U_{ij}^{p-2} is a $(p-2)th$ order approximation of u, i.e., there exists $z(r, \theta)$ sufficiently smooth and bounded on the closure of Ω^- such that

$$U_{ij}^{p-2} = u(r_i, \theta_j) + h^{p-2} z(r_i, \theta_j), \qquad \textit{with} \quad h = \max\{\Delta r, \Delta\theta\}. \qquad (2.31)$$

The following lemma is the analogue of Lemma 2.5 for a p ordered scheme.

Lemma 2.7. *For U_{ij}^{p-2} and $u(r, \theta)$ satisfying the hypothesis of Theorem 2.6, it holds that the standard $(p+2-q)th$ order centered finite difference operator:*

(i) D_{qr}^{p+2-q} *acting on* U_{ij}^{p-2} *is consistent with the derivative* u_{qr} *of order* $\mathcal{O}(h^{p+2-q})$, *for* $q = 4, 6 \dots, p$.

(ii) $D_{(q-1)r}^{p+2-q}$ *acting on* U_{ij}^{p-2} *is consistent with the derivative* $u_{(q-1)r}$ *of order* $\mathcal{O}(h^{p+2-q})$, *for* $q = 4, 6 \dots, p$.

(iii) $D_{q\theta}^{p+2-q}$ *acting on* U_{ij}^{p-2} *is consistent with the derivative* $u_{q\theta}$ *of order* $\mathcal{O}(h^{p+2-q})$, *for* $q = 4, \dots, p$.

Proof. To prove (i), I apply D_{qr}^{p+2-q} to U_{ij}^{p-2} and use (2.31). This leads to

$$\begin{aligned} D_{qr}^{p+2-q}U_{ij}^{p-2} &= D_{qr}^{p+2-q}u_{ij} + h^{p-2}D_{qr}^{p+2-q}z_{ij} \\ &= (u_{qr})_{ij} + \mathcal{O}(h^{p+2-q}) + h^{p-2}(z_{qr})_{ij} + \mathcal{O}(h^{2p-q}) \end{aligned}$$

Therefore,

$$D_{qr}^{p+2-q}U_{ij}^{p-2} = (u_{qr})_{ij} + \mathcal{O}(h^{p+2-q}), \tag{2.32}$$

for $q = 4, 6 \ldots, p$. The proofs of parts (ii) and (iii) follow the same pattern. □

Now, I am ready to prove Theorem 2.6

Proof. (Proof of Theorem 2.6)

First, I rewrite $\mathcal{H}^p U_{ij}$ as

$$\begin{aligned} \mathcal{H}^p U_{ij} =& D_{2r}^2 U_{ij} - \frac{2h^2}{4!}D_{4r}^{p-2}U_{ij}^{p-2} - \frac{2h^4}{6!}D_{6r}^{p-4}U_{ij}^{p-2} - \ldots - \frac{2h^{p-2}}{p!}D_{pr}^2 U_{ij}^{p-2} \\ &+ \frac{1}{r_i}\left(D_r^2 U_{ij} - \frac{h^2}{3!}D_{3r}^{p-2}U_{ij}^{p-2} - \frac{h^4}{5!}D_{5r}^{p-4}U_{ij}^{p-2} - \ldots - \frac{h^{p-2}}{(p-1)!}D_{(p-1)r}^2 U_{ij}^{p-2}\right) \\ &+ \frac{1}{r_i^2}\left(D_{2\theta}^2 U_{ij} - \frac{2h^2}{4!}D_{4\theta}^{p-2}U_{ij}^{p-2} - \frac{2h^4}{6!}D_{6\theta}^{p-4}U_{ij}^{p-2} - \ldots - \frac{2h^{p-2}}{p!}D_{p\theta}^2 U_{ij}^{p-2}\right) + k^2 U_{ij}. \end{aligned}$$

Then applying $\mathcal{H}^p$ to u, which satisfy (2.31), and expanding the individual terms where the discrete operators act on u_{ij} results in

$$
\begin{aligned}
\mathcal{H}^p u_{ij} = {} & (u_{rr})_{ij} + \frac{2h^2}{4!}\,(u_{4r})_{ij} + \ldots + \frac{2h^{p-2}}{p!}(u_{pr})_{ij} + \mathcal{O}(h^p) \\
& - \frac{2h^2}{4!} D_{4r}^{p-2} U_{ij}^{p-2} - \ldots - \frac{2h^{p-2}}{p!} D_{pr}^2 U_{ij}^{p-2} \\
& + \frac{1}{r_i}\Bigg((u_r)_{ij} + \frac{h^2}{3!}\,(u_{3r})_{ij} + \ldots + \frac{h^{p-2}}{(p-1)!}\left(u_{(p-1)r}\right)_{ij} + \mathcal{O}(h^p) \\
& -\frac{h^2}{3!} D_{3r}^{p-2} U_{ij}^{p-2} - \ldots - \frac{h^{p-2}}{(p-1)!} D_{(p-1)r}^2 U_{ij}^{p-2} \Bigg) \\
& + \frac{1}{r_i^2}\Bigg((u_{\theta\theta})_{ij} + \frac{2h^2}{4!}\,(u_{4\theta})_{ij} + \ldots + \frac{2h^{p-2}}{p!}(u_{p\theta})_{ij} + \mathcal{O}(h^p) \\
& -\frac{2h^2}{4!} D_{4\theta}^{p-2} U_{ij}^{p-2} - \ldots - \frac{2h^{p-2}}{p!} D_{p\theta}^2 U_{ij}^{p-2} \Bigg) + k^2 u_{ij}.
\end{aligned}
$$

Reordering and appropriately combining terms yields

$$
\begin{aligned}
\mathcal{H}^p u_{ij} = {} & (u_{rr})_{ij} + \frac{1}{r_i}(u_r)_{ij} + \frac{1}{r_i^2}(u_{\theta\theta})_{ij} + k^2 u_{ij} \\
& - \frac{2h^2}{4!}\left(D_{4r}^{p-2} U_{ij}^{p-2} - (u_{4r})_{ij} \right) - \ldots - \frac{2h^{p-2}}{p!}\left(D_{pr}^2 U_{ij}^{p-2} - (u_{pr})_{ij} \right) \\
& - \frac{h^2}{3! r_i}\left(D_{3r}^{p-2} U_{ij}^{p-2} - (u_{3r})_{ij} \right) - \ldots - \frac{h^{p-2}}{(p-1)! r_i}\left(D_{(p-1)r}^2 U_{ij}^{p-2} - \left(u_{(p-1)r}\right)_{ij} \right) \\
& - \frac{2h^2}{4! r_i^2}\left(D_{4\theta}^{p-2} U_{ij}^{p-2} - (u_{4\theta})_{ij} \right) - \ldots - \frac{2h^{p-2}}{p! r_i^2}\left(D_{p\theta}^2 U_{ij}^{p-2} - (u_{p\theta})_{ij} \right) + \mathcal{O}(h^p).
\end{aligned}
$$

Thus, applying the statements of Lemma 2.7 to each of the expressions in parentheses yields

$$
\mathcal{H}^p u_{ij} = \left(\Delta_{r\theta} u + k^2 u \right)_{ij} + \mathcal{O}(h^p),
$$

which finishes the proof. □

2.3.4 Arbitrary order DC approximation for the KFE.

Following the derivation described in the previous three sections, I can obtain arbitrary order DC approximations for the KFE at the grid points (r_N, θ_j) by using appropriate one-sided finite difference for the derivatives present in the truncation error terms. For instance, the definitions of the pth order approximations for (2.9) and (2.10) are natural extensions of (2.22)-(2.23). They consist of adding discrete approximations to the continuous derivatives present in all the truncation error terms up to the pth order.

$$\begin{aligned}\frac{U^p_{N+1,j}-U^p_{N-1,j}}{2\Delta r} &- \left.\partial_r\left(H_0(kr)\sum_{l=0}^{L-1}\frac{F^p_{lj}}{r^l}+H_1(kr)\sum_{l=0}^{L-1}\frac{G^p_{lj}}{r^l}\right)\right|_{r=r_N=R} \qquad (2.33)\\ &= \frac{h^2}{3!}(Dl)^{p-2}_{3r}U^{p-2}_{ij}+\frac{h^4}{5!}(Dl)^{p-4}_{5r}U^{p-2}_{ij}+\ldots+\frac{h^{p-2}}{(p-1)!}(Dl)^2_{(p-1)r}U^{p-2}_{ij}\\ \frac{U^p_{N+1,j}-2U^p_{Nj}+U^p_{N-1,j}}{\Delta r^2} &- \left.\partial^2_r\left(H_0(kr)\sum_{l=0}^{L-1}\frac{F^p_{lj}}{r^l}+H_1(kr)\sum_{l=0}^{L-1}\frac{G^p_{lj}}{r^l}\right)\right|_{r=r_N=R} \qquad (2.34)\\ &= \frac{2h^2}{4!}(Dl)^{p-2}_{4r}U^{p-2}_{ij}+\frac{2h^4}{6!}(Dl)^{p-4}_{6r}U^{p-2}_{ij}+\ldots+\frac{2h^{p-2}}{p!}(Dl)^2_{pr}U^{p-2}_{ij}.\end{aligned}$$

In the discrete equations (2.33)-(2.34), I employ $(p+2-q)$th order discrete finite difference operators, $(Dl)^{p+2-q}_{(q-1)r}$ and $(Dl)^{p+2-q}_{qr}$ (for $q=4,6,\cdots,p$) acting on the discrete function U^{p-2}_{ij} approximating u of order $(p-2)$th. The use of Dl instead of D states that left one-sided finite difference approximations of the corresponding continuous derivatives are used.

Analogously, I formulate pth order approximations of the recurrence formulas as

$$\begin{aligned}2lG^p_{lj}-(l-1)^2F^p_{l-1,j} &- \frac{F^p_{l-1,j+1}-2F^p_{l-1,j}+F^p_{l-1,j-1}}{\Delta\theta^2} \qquad (2.35)\\ &= -\frac{2h^2}{4!}D^{p-2}_{4\theta}F^{p-2}_{l-1,j}-\frac{2h^4}{6!}D^{p-4}_{6\theta}F^{p-2}_{l-1,j}-\ldots-\frac{2h^{p-2}}{p!}D^2_{p\theta}F^{p-2}_{l-1,j},\\ 2lF^p_{lj}+l^2G^p_{l-1,j} &+ \frac{G^p_{l-1,j+1}-2G^p_{l-1,j}+G^p_{l-1,j-1}}{\Delta\theta^2} \qquad (2.36)\\ &= \frac{2h^2}{4!}D^{p-2}_{4\theta}G^{p-2}_{l-1,j}+\frac{2h^4}{6!}D^{p-4}_{6\theta}G^{p-2}_{l-1,j}+\ldots+\frac{2h^{p-2}}{p!}D^2_{p\theta}G^{p-2}_{l-1,j},\end{aligned}$$

where $F^{p-2}_{l-1,j}$ and $G^{p-2}_{l-1,j}$ are part of the previously calculated $(p-2)$th ordered numerical solution, and the discrete operators $D^{p+2-q}_{q\theta}$ are centered finite difference operators. Summarizing, the set of equations (2.29), (2.33)-(2.34), (2.35)-(2.36), the discrete version of the continuity of the scattered field (2.8), and the appropriate discretization of the boundary condition at the obstacle (2.7) form the pth order DC discrete system of equations to be solved. I denote this system as *KDCp*.

2.4 STANDARD FOURTH ORDER NUMERICAL METHOD FOR THE KFE-BVP

In this section, I formulate a standard fourth order numerical method for the KFE-BVP (2.6)-(2.12) in polar coordinates. This constitutes an alternative high order method for this BVP. In Section 2.6, I compare it with the DC fourth order method and assess convergence, accuracy and computational efficiency of both. This fourth order method is also a natural extension of the standard second order finite difference method, carefully constructed in [17], where the KFE was first introduced.

I begin by considering the centered 9-point standard finite difference scheme for the Helmholtz equation in polar coordinates,

$$\begin{aligned}\mathcal{H}_9 \bar{U}^4_{ij} \equiv & \frac{-\bar{U}^4_{i+2,j} + 16\bar{U}^4_{i+1,j} - 30\bar{U}^4_{i,j} + 16\bar{U}^4_{i-1,j} - \bar{U}^4_{i-2,j}}{12\Delta r^2} \\ & + \frac{1}{r_i}\left(\frac{-\bar{U}^4_{i+2,j} + 8\bar{U}^4_{i+1,j} - 8\bar{U}^4_{i-1,j} + \bar{U}^4_{i-2,j}}{12\Delta r}\right) \\ & + \frac{1}{r_i^2}\left(\frac{-\bar{U}^4_{i,j+2} + 16\bar{U}^4_{i,j+1} - 30\bar{U}^4_{i,j} + 16\bar{U}^4_{i,j-1} - \bar{U}^4_{i,j-2}}{12\Delta\theta^2}\right) + k^2\bar{U}^4_{ij} = 0. \end{aligned} \tag{2.37}$$

at the interior gridlines $r_2 < r_i < r_{N-1}$. I adopt the alternative notation for the standard fourth order numerical solution $\bar{U}^4_{ij}$, because it is different from its DC counterpart U^4_{ij}, as confirmed by my numerical results in the next section. At the boundaries of the domain, appropriate fourth order one-sided finite difference approximations of the various derivatives of the Helmholtz equation are required.

I also need non-centered fourth order finite difference approximations for the various equations of the KFE. For instance,

(i) Continuity of the first derivative at the artificial boundary:

$$\begin{aligned}&\frac{1}{\Delta r}\left[\frac{1}{4}\bar{U}^4_{N+1,j} + \frac{5}{6}\bar{U}^4_{N,j} - \frac{3}{2}\bar{U}^4_{N-1,j} + \frac{1}{2}\bar{U}^4_{N-2,j} - \frac{1}{12}\bar{U}^4_{N-3,j}\right] \\ &\qquad - \partial_r\left(H_0(kr)\sum_{l=0}^{L-1}\frac{\bar{F}^4_{lj}}{r^l} + H_1(kr)\sum_{l=0}^{L-1}\frac{\bar{G}^4_{lj}}{r^l}\right)_{r=r_N} = 0.\end{aligned} \tag{2.38}$$

(ii) Continuity of the second derivative at the artificial boundary:

$$\frac{1}{\Delta r^2}\left[\frac{5}{6}\bar{U}^4_{N+1,j}-\frac{5}{4}\bar{U}^4_{N,j}-\frac{1}{3}\bar{U}^4_{N-1,j}+\frac{7}{6}\bar{U}^4_{N-2,j}-\frac{1}{2}\bar{U}^4_{N-3,j}+\frac{1}{12}\bar{U}^4_{N-4,j}\right] \\ -\ \partial_r^2\left(H_0(kr)\sum_{l=0}^{L-1}\frac{\bar{F}^4_{lj}}{r^l}+H_1(kr)\sum_{l=0}^{L-1}\frac{\bar{G}^4_{lj}}{r^l}\right)_{r=r_N}=0. \tag{2.39}$$

(iii) Standard fourth order discretization of the recursion formulas along the angular direction:

$$2l\bar{G}^4_{lj}-(l-1)^2\bar{F}^4_{l-1,j}-\frac{-\bar{F}^4_{l-1,j+2}+16\bar{F}^4_{l-1,j+1}-30\bar{F}^4_{l-1,j}+16\bar{F}^4_{l-1,j-1}-\bar{F}^4_{l-1,j-2}}{12\Delta r^2}=0, \tag{2.40}$$

$$2l\bar{F}^4_{lj}+l^2\bar{G}^4_{l-1,j}+\frac{-\bar{G}^4_{l-1,j+2}+16\bar{G}^4_{l-1,j+1}-30\bar{G}^4_{l-1,j}+16\bar{G}^4_{l-1,j-1}-\bar{G}^4_{l-1,j-2}}{12\Delta r^2}=0, \tag{2.41}$$

for $l = 1, \dots L-1$. Again, I have adopted the alternative notation for the standard fourth order numerical solutions $\bar{F}^4$, and $\bar{G}^4$ to differentiate them from their DC fourth order counterparts F^4, and G^4, respectively. Notice that I have retained the values of the unknown functions at the ghost points (r_{N+1}, θ_j) in all the one-sided finite difference approximations. As a consequence another set of unknowns is added to the problem. However, they are eliminated considering an additional set of equations given by the discretization of the Helmholtz equation (2.37) at the nodes located on the artificial boundary $r = r_N$. My numerical experiments suggests that this practice leads to a more accurate and stable numerical solutions than just using typical one-sided finite differences. The set of equations (2.37)-(2.41) and the discrete version of the continuity u (2.8) at the artificial boundary form the standard 4th order method for the KFE-BVP (2.6)-(2.12). I will denote this method as *KS4*.

At the computational level, this fourth order standard method reduces to a new linear system of equations (LSE) given by

$$A_4\bar{\mathbf{U}}^4 = \mathbf{b}. \tag{2.42}$$

This matrix A_4 has a greater number of nonzero entries than the matrix associated to the fourth order DC method described above. As a consequence, memory and computing costs increase for this standard formulation. In Section (2.6), I compare both fourth order techniques through some numerical experiments.

2.5 IMPLEMENTATION OF THE DC NUMERICAL METHOD TO THE KFE-BVP

The practical advantage of the DC method coupled with the KFE is that it leads to arbitrary high order numerical approximations to the solution of scattering BVPs, such as (2.6)-(2.12). Here, I choose an obstacle of circular shape to alleviate the transformation of the KFE-BVP into a linear system. As mentioned before, in Section 4, I discuss the scattering from arbitrarily shaped scatterers. My strategy to generate a pth order DC numerical approximation U_{ij}^{p} to the exact solution u of the BVP (2.6)-(2.12) can be summarized by the following steps:

(i) Obtain a second order approximation U_{ij}^{2} to the exact solution u using a standard second order finite difference technique for the Helmholtz equation and the BCs. This technique was adopted in [17]. As shown there, the set of discrete equations employed to obtain U_{ij}^{2} can be recast into the LSE,

$$A_2\mathbf{U}^2 = \mathbf{b}. \tag{2.43}$$

In particular, the vector $\mathbf{U}^2$ consists of the unknown discrete value approximations of the scattered field u, and the unknown angular coefficients of the Karp's expansion for a given grid. The vector $\mathbf{b}$ is assembled from the boundary data at the obstacle obtained from the incident wave. More precisely, the unknown vector $\mathbf{U}^2$ is defined as

$$\begin{aligned}\mathbf{U}^2 = \Big[& \overbrace{U^2_{1,1}\ldots U^2_{1,m}}^{\text{at obstacle}} \;\; \overbrace{U^2_{2,1}\ldots U^2_{2,m}\ldots U^2_{N-1,1}\ldots U^2_{N-1,m}}^{\text{at interior grid points}} \\ & \overbrace{F^2_{0,1}\ldots F^2_{0,m}\, G^2_{0,1}\ldots G^2_{0,m}\ldots\, F^2_{L-1,1}\ldots F^2_{L-1,m}\, G^2_{L-1,1}\ldots G^2_{L-1,m}}^{\text{at artificial boundary}} \Big]^T,\end{aligned} \tag{2.44}$$

and the vector **b**, for a Dirichlet boundary condition on the obstacle, as

$$\mathbf{b} = \Big[\overbrace{-(u_{inc})_{1,1} \ldots - (u_{inc})_{1,m}}^{\text{at obstacle}} \quad \overbrace{0 \ldots 0 \ldots 0 \ldots 0}^{\text{at interior grid points}} \quad \overbrace{0 \ldots 0 \ldots 0 \ldots 0}^{\text{at artificial boundary}} \Big]^T. \tag{2.45}$$

Thus, the LSE dimension is $(N-1+2L)m \times (N-1+2L)m$ where the first $m \times m$ block of the matrix A_2 corresponds to the identity matrix. In the case of a Neumann BC, minor updates to the m first equations should be made. Specifically, A_2 is affected by the ghost-point based treatment of the discretization of the radial derivative in (2.7), and $\mathbf{b}$ depends on the boundary data $\partial_r u_{\text{inc}}$. See details in Appendix B.

The sparse structure of the matrix A_2 is studied in [17], where built-in MATLAB linear solvers were employed to obtain second order accurate solutions. In fact, the complex matrix A_2 is non-Hermitian and its condition number worsens as the number of KFE terms increases, or the discretization grid is refined. More precisely, the standard discretization of the KFE and the ordering of the discrete unknowns in $\mathbf{U}^2$ leads to a highly asymmetric block structure of the lower non-zero coefficients of A_2. Nevertheless in [17], the LU MATLAB solvers were successfully used for an ample set of scattering problems whose discretization ended in the LSE (2.43). In this work, I also employ the direct built-in MATLAB linear solvers for my two dimensional high order DC schemes. As it is seen in my numerical experiments in Section 6, I obtained excellent high order approximations for very refined grids up to 60 PPW and up to a maximum of 12 terms in the Karp's fafrfield expansion.

(ii) Construct a fourth order finite difference DC consistent scheme of the Helmholtz equation by subtracting the second order leading terms of the truncation errors from the second order standard scheme (2.13). This leads to the desired fourth order finite difference deferred correction discrete equation (2.19) consistent with the Helmholtz equation. Likewise, obtain fourth order approximations to the boundary conditions (2.8)-(2.12). For this purpose, use appropriate approximations to the various continuous derivatives present in the leading order truncation error terms using the second order approximation U_{ij}^2 obtained in step (a). This process is described in detail in sections 2.3.1-2.3.2. The resulting linear system is given by

$$A_2\mathbf{U}^4 = \mathbf{b} + \mathbf{b}^4_{DC}(\mathbf{U}^2). \tag{2.46}$$

The unknown vector $\mathbf{U}^4$ is identical to $\mathbf{U}^2$ in (2.43), except in the replacement of the superscript number 2 by 4. Also, the dependence of the correction vector $\mathbf{b}^4_{DC}$ on the second order numerical solution has been made explicit. This new vector consists of all the corrections in (2.19), (2.22), (2.23), (2.26) and (2.27). In the particular case of Dirichlet BC, it reads

$$\begin{gathered}
\mathbf{b}^4_{DC}(\mathbf{U}^2) = \Big[\ \overbrace{0\cdots0}^{\text{at boundary}} \quad \overbrace{\frac{\Delta r^2}{12}\left(D^2_{4r}U^2_{2,1} + \frac{2}{r_2}D^2_{3r}U^2_{2,1}\right) + \frac{\Delta\theta^2}{12r_2^2}D^2_{4\theta}U^2_{2,1}\cdots}^{\text{at interior grid points}} \\
\overbrace{\frac{\Delta r^2}{12}\left(D^2_{4r}U^2_{N-1,m} + \frac{2}{r_{N-1}}D^2_{3r}U^2_{N-1,m}\right) + \frac{\Delta\theta^2}{12r_{N-1}^2}D^2_{4\theta}U^2_{N-1,m}}^{\text{at interior grid points (continued)}} \\
\overbrace{\frac{\Delta r^2}{12}\left((Dl)^2_{4r}U^2_{N,1} + \frac{2}{r_N}(Dl)^2_{3r}U^2_{N,1}\right) + \frac{\Delta\theta^2}{12r_N^2}(Dl)^2_{4\theta}U^2_{N,1} - \left(\frac{\Delta r}{3} + \frac{\Delta r^2}{6r_N}\right)(Dl)^2_{3r}U^2_{N,1}\cdots}^{\text{at artificial boundary}} \\
\overbrace{\frac{\Delta r^2}{12}\left((Dl)^2_{4r}U^2_{N,m} + \frac{2}{r_N}(Dl)^2_{3r}U^2_{N,m}\right) + \frac{\Delta\theta^2}{12r_N^2}(Dl)^2_{4\theta}U^2_{N,m} - \left(\frac{\Delta r}{3} + \frac{\Delta r^2}{6r_N}\right)(Dl)^2_{3r}U^2_{N,m}}^{\text{at artificial boundary (continued)}} \\
\overbrace{\frac{\Delta r^2}{12}(Dl)^2_{4r}U^2_{N,1} - \frac{\Delta r}{3}(Dl)^2_{3r}U^2_{N,1}\cdots\frac{\Delta r^2}{12}(Dl)^2_{4r}U^2_{N,m} - \frac{\Delta r}{3}(Dl)^2_{3r}U^2_{N,m}}^{\text{at artificial boundary (continued)}} \\
\overbrace{-\frac{\Delta\theta^2}{12}D^2_{4\theta}F^2_{0,1}\cdots-\frac{\Delta\theta^2}{12}D^2_{4\theta}F^2_{0,m}\ \frac{\Delta\theta^2}{12}D^2_{4\theta}G^2_{0,1}\cdots\frac{\Delta\theta^2}{12}D^2_{4\theta}G^2_{0,m}}^{\text{at artificial boundary (continued)}}\cdots \\
\overbrace{-\frac{\Delta\theta^2}{12}D^2_{4\theta}F^2_{L-1,1}\cdots-\frac{\Delta\theta^2}{12}D^2_{4\theta}F^2_{L-1,m}\ \frac{\Delta\theta^2}{12}D^2_{4\theta}G^2_{L-1,1}\cdots\frac{\Delta\theta^2}{12}D^2_{4\theta}G^2_{L-1,m}}^{\text{at artificial boundary (continued)}}\Big]^T.
\end{gathered} \tag{2.47}$$

Alternatively, under Neumann conditions, the first m components of this vector must account for the correction term (B.1), in Appendix B combined to those arising from the ghost-point boundary treatment. By solving the linear system (2.46), I obtain a fourth order numerical approximation, U^4_{ij}, of the solution u of the original BVP. An important aspect of this approach is that the matrix A_2 remains the same in both the second and fourth order computations. The only change occurs in the forcing term.

(iii) Continue the iterative construction process described in (b) until a desired pth order approximation U_{ij}^{p} of the exact solution u is obtained from the previous approximation U_{ij}^{p-2}. The associated linear system in this general case is given by

$$A_2\mathbf{U}^p = \mathbf{b} + \mathbf{b}_{DC}^{p}(\mathbf{U}^{p-2}). \tag{2.48}$$

The components of the vector $\mathbf{b}_{DC}^{p}$ consists of the approximations of the high order correction terms present in (2.29), (2.33), (2.34), (2.35) and (2.36). All of them are computed from $\mathbf{U}^{p-2}$. The unknown vector $\mathbf{U}^p$ is identical to $\mathbf{U}^2$ in (2.43), by replacing 2 by p in all its components. Therefore, to obtain a numerical solution approximating the exact solution two orders higher, it is required to solve an additional linear system. However, all the linear systems to be solved using the DC technique have the same sparse matrix A_2. The difference is in the forcing terms as explained above. Compared to high order standard schemes, this DC implementation feature is advantageous regardless of the adopted LSE resolution strategy. In the case of direct solvers, A_2 factorization is performed once and then reused throughout the high order DC iteration. In the case of iterative solvers, all the linear systems to be solved as part of the DC iteration use the same solving algorithm, under the same preconditioning and optimal implementation. Therefore, the resolution strategy requires a one-time computational investment over a rather simple matrix for every DC iteration step.

In Section 2.6, I perform numerical experiments employing the discrete DC Helmholtz operators $\mathcal{H}^4$ and $\mathcal{H}^6$ of fourth and sixth order, respectively. As a result, I obtain numerical solutions approximating the scattered field u of the KFE-BVP (2.6)-(2.12). By comparing these numerical solutions against the corresponding exact solutions for circular scatterers, the expected fourth and sixth order of convergence, respectively, are achieved. For completeness, several of the sixth order finite difference formulas, used in this work, approximating continuous derivatives are given in the Appendix A. These continuous derivatives are contained in the leading order truncation error terms of the finite difference approximations of the Helmholtz equation and the equations forming the KFE, respectively. Also, the deferred corrections approximations for the Neumann boundary condition are given in the Appendix B.

2.6 NUMERICAL RESULTS

In this section, I discuss numerical results for the scattering of a time harmonic incident plane wave, $\hat{u}_{inc}(\mathbf{x}, t) = e^{-i\omega t}e^{ikx} = e^{i\omega t}u_{inc}(\mathbf{x})$ propagating in the direction of the positive x-axis, from a circular obstacle. I obtain numerical solutions for my proposed deferred correction method coupled with the Karp's farfield expansion ABC, which is applied to the KFE-BVP defined by (2.6)-(2.12). To access the high accuracy and high order of convergence of this technique, I compare my numerical results to the exact solution of the exterior BVP defined by (2.1)-(2.3) for a circular obstacle of radius r_0 and wavenumber k. The exact solution for the scattered field u and its corresponding *Farfield Pattern* (FFP), $P(\theta)$ are as follows:

(i) Dirichlet boundary condition: $u = -u_{inc}$,

$$u(r, \theta) = -\sum_{n=0}^{\infty} \epsilon_n i^n \frac{J_n(kr_0)}{H_n^{(1)}(kr_0)} H_n^{(1)}(kr) \cos n\theta \tag{2.49}$$

$$P(\theta) = -\left(\frac{2}{k\pi}\right)^{1/2} e^{-i\pi/4} \sum_{n=0}^{\infty} \epsilon_n \frac{J_n(kr_0)}{H_n^{(1)}(kr_0)} \cos n\theta, \tag{2.50}$$

(ii) Neumann boundary condition: $\partial_n u = -\partial_n u_{\text{inc}}$,

$$u(r, \theta) = -\sum_{n=0}^{\infty} \epsilon_n i^n \frac{J_n'(kr_0)}{H_n'^{(1)}(kr_0)} H_n^{(1)}(kr) \cos n\theta \tag{2.51}$$

$$P(\theta) = -\left(\frac{2}{k\pi}\right)^{1/2} e^{-i\pi/4} \sum_{n=0}^{\infty} \epsilon_n \frac{J_n'(kr_0)}{H_n'^{(1)}(kr_0)} \cos n\theta, \tag{2.52}$$

where $\epsilon_0 = 1$ and $\epsilon_n = 2$ for $n \geq 1$.

In Fig. 2.1, I show some numerical results obtained by applying the fourth order deferred correction technique KDC4, introduced in Sections 2.3.1-2.3.2, to the KFE-BVP. The left graphs illustrate the amplitude of the total field, $u_{total} = u_{inc} + u$ for both boundary conditions. The middle graphs shows the comparison of the numerical Farfield Patterns (defined below) against the exact ones. The rightmost graphs show the fourth order of convergence of the numerical solution to the exact solution. In both numerical experiments, the wavelength is 2π, the number of Karp Expansion terms is 9, the outer radius is 3, and the number of gridpoints per wavelength to determine the order of convergence is $[20, 30, 40, 50, 60]$. The infinite series defining the exact solutions have been truncated to 60 terms for my calculations. In the following subsections, I present numerous results for the application of the DC technique to the KFE-BVP for the two BCs under studied. Discussion of the order of convergence and accuracy of the DC techniques, along with comparisons against other high order techniques are included as well.

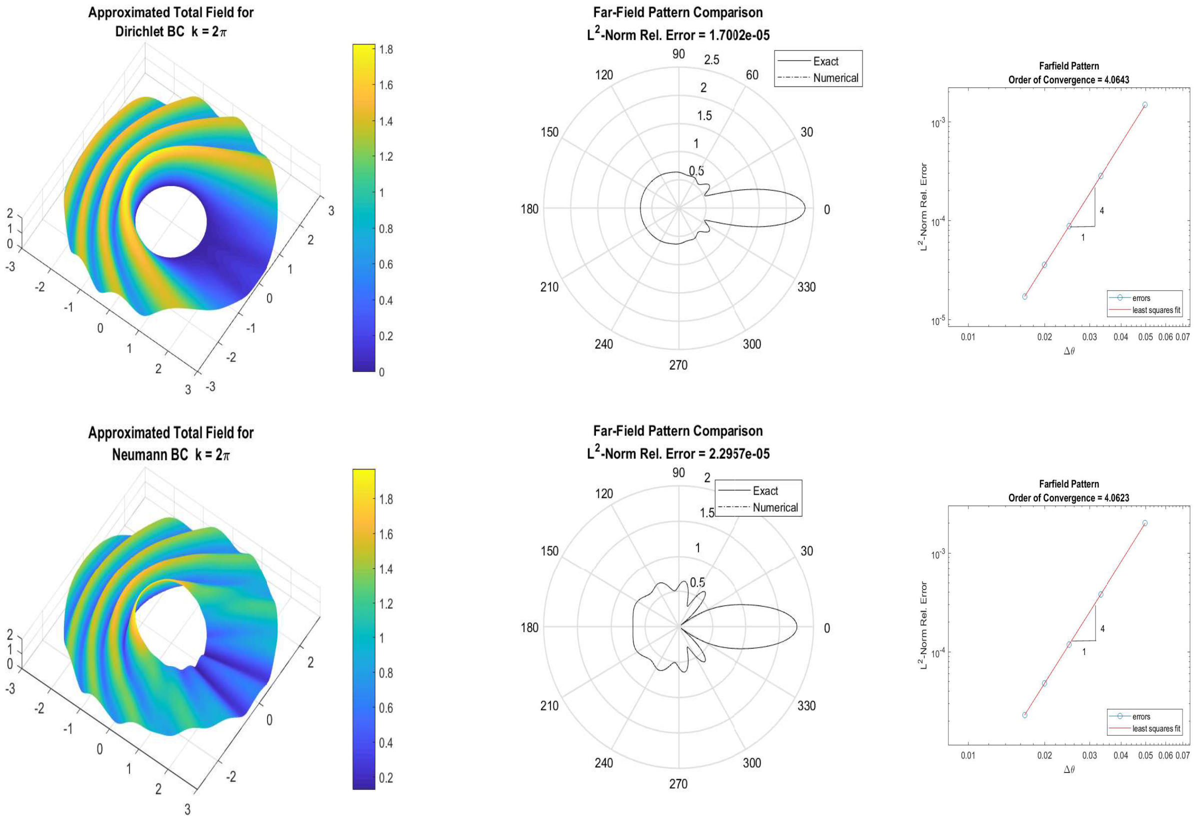

Figure 2.1: Numerical results for scattering from a circular scatterer using KFE. Shown from left to right are the wave amplitude, Farfield Pattern, and order of convergence for Dirichlet (top) and Neumann (bottom) BCs.

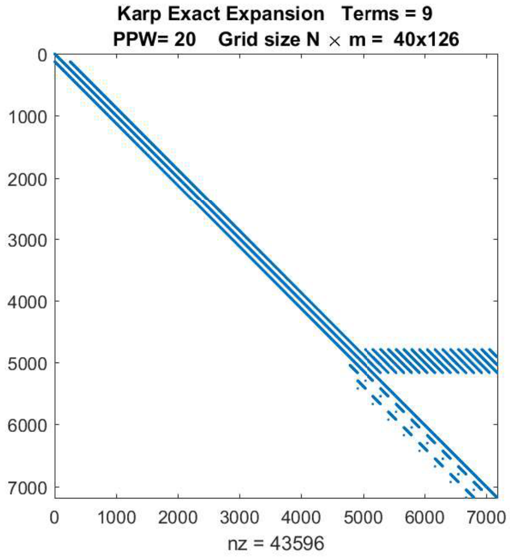

Figure 2.2: Matrix density for the matrix used in the solution of the first image shown in Figure 2.1

2.6.1 Accuracy and convergence under Dirichlet BC. I perform several numerical experiments to obtain approximations of the FFP of the scattered wave for the BVP (2.6)-(2.12) under Dirichlet boundary conditions. The FFP is an important property to be analyzed in scattering problems. It depends on the shapes and physical properties of the scatterers. In Section 4.2.1 of [25], Martin defines the Farfield Pattern (FFP) as the angular function present in the dominant term of the asymptotic expansions for the scattered wave when $r \to \infty$. For instance, in 2D, the Farfield Pattern is the coefficient $f_0(\theta)$ of the leading order term of the asymptotic approximation of Karp expansion,

$$u(r,\theta) = \frac{e^{ikr}}{(kr)^{1/2}} f_0(\theta) + O\left(1/(kr)^{3/2}\right). \tag{2.53}$$

Following Bruno and Hyde [26], I calculate it from the approximation of the scattered wave at the artificial boundary. A detailed computation is found in [17].

In my first set of experiments, I obtain the L^2 norm relative errors made by approximating the exact FFP by the numerical FFP using both the DC and standard techniques. In all these experiments, the wavenumber is $k = 2\pi$ and the radius of the circular obstacle is $r_0 = 1$ while the radius of the artificial boundary is either $R = 2$ or $R = 3$. To determine the convergence rates of the numerical solutions to the exact solution, I refine my polar grid by increasing the number of gridpoints per wavelength (PPW) from 20 to 60. These results are illustrated in Figs. 2.3 and 2.4. In Fig. 2.3, I present four cases with varying number of Karp Expansion terms, NKFE = 4,8,10,13 while the grid is systematically refined. In these figures, I denote solutions using the DC methods of fourth and sixth order as KDC4 and KDC6, respectively. Also, those solutions obtained from the application of the standard second and fourth order schemes are referred to as KS2 and KS4, respectively.

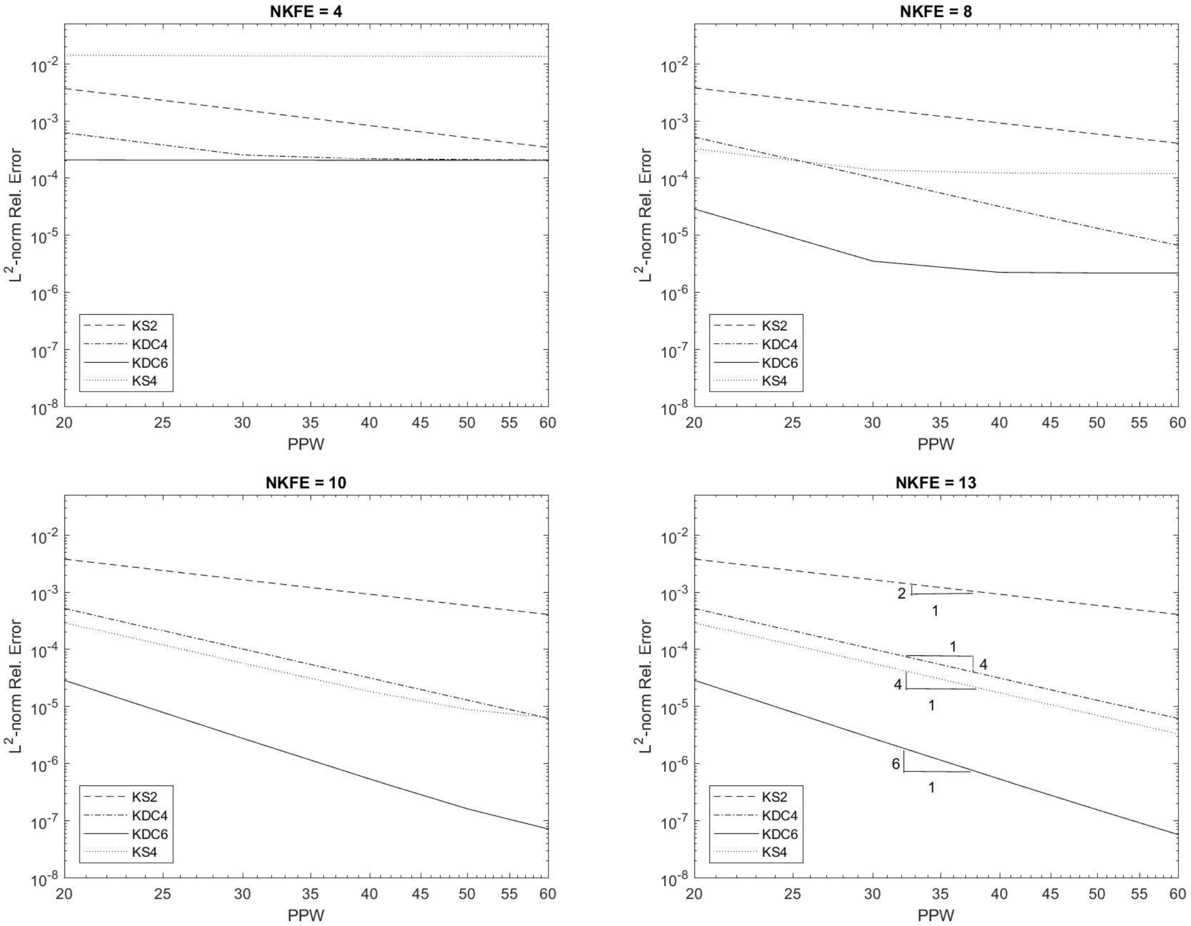

Figure 2.3: Comparison of L^2-norm relative errors of the Farfield Pattern computed from KS2, KDC4, KDC6 and KS4 methods for $R = 2$

An analysis of the graphs in Fig. 2.3 reveals how the accuracy and convergence rate of the standard and DC techniques, coupled with the KFE, depend on both PPW and the number of Karp's expansion terms. From the top left plot of Fig. 2.3, it is observed that the only method

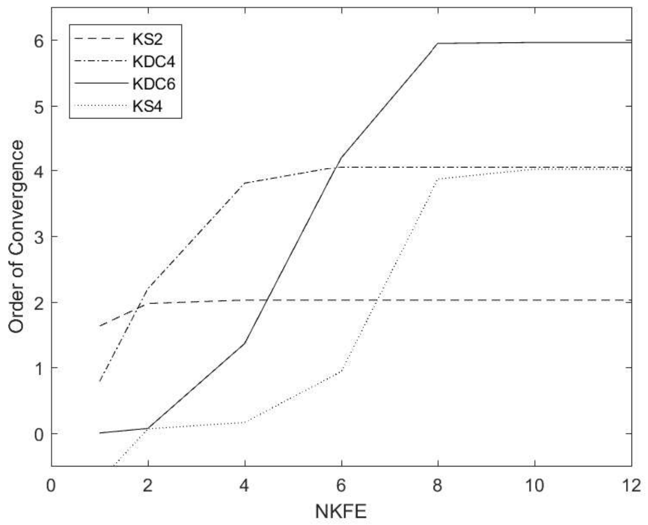

Figure 2.4: Comparison of convergence rates between the DC and standard methods in terms of NKFE.

that attains the expected convergence rate (2nd order convergence), when NKFE = 4, is KS2. Furthermore, KDC4 seems to attain the expected convergence rate only for coarser grids, while errors of the other methods remain nearly constant as PPW increases. As NKFE increases from 4 to 8 terms (top right plot of Fig. 2.3), I observe that KS2 continues attaining the second order rate, but now KDC4 also achieves the expected 4th order convergence rate along the full PPW range. However, KDC6 and KS4 convergence rates improve for the coarser grids, but as I continue refining, they degrade quickly. More consistent experimental results are attained by all methods for 10 KFE terms, as depicted in the bottom left plot of Fig. 2.3, with the exception of KS4 whose order drops slightly below 4 for the finer grids. Finally for NKFE = 13, all these methods attain their theoretical convergence rate, as shown in the bottom right plot of Fig. 2.3, this can be more clearly seen for the 4th order DC scheme in Table 2.1.

Alternatively, Fig. 2.4 shows the convergence rates attained by the DC and the standard methods as the number of terms in Karp expansion (NKFE) increases. In these experiments, the artificial boundary is located at $R = 3$ and the various grids used to determine the convergence rate consist of PPW = 20, 30, 40, 50 and 60. It is seen from Figs. 2.3 and 2.4 that any of these four methods can reach its theoretical order of convergence, if enough terms in Karp's expansion are retained

PPW	Grid size	$h = \Delta\theta = \Delta r$	L^2-norm Rel. Error	Observed order
20	20×126	0.04987	5.69×10^{-4}	
30	30×189	0.03324	1.09×10^{-4}	4.08
40	40×252	0.02493	3.39×10^{-5}	4.04
50	50×315	0.01995	1.38×10^{-5}	4.02
60	60×377	0.01667	6.69×10^{-6}	4.04

Table 2.1: Order of convergence of 4th order scheme shown in the fourth plot of Figure 2.3.

for sufficiently fine grids. This fact illuminates the arbitrary high order character of the KFE-ABC, whose accuracy is easily adjustable to the precision of the interior Helmholtz solver. In addition, the order of convergence of the proposed interior scheme can be efficiently increased by adding higher order error terms of the discretized Helmholtz differential operator into the DC numerical scheme.

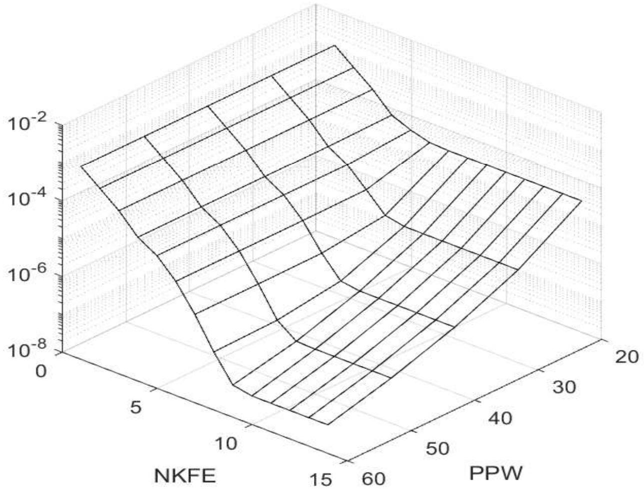

Figure 2.5: L^2-norm FFP relative error employing KDC6 method for various numbers of Karp's expansion terms and PPW values. Problem parameters are $r_0 = 1$, $k = 2\pi$, $R = 2$.

The dependence of the L^2-norm FFP relative error on PPW and NKFE is explored in Fig. 2.5 for the KDC6 method. Note that at coarser grids, increasing the number of Karp's expansion terms only leads to minor accuracy improvements. On the contrary, as the grids become more refined using larger NKFE, greater accuracy occurs. In fact, for NKFE $= 8$, the L^2 relative error approaches 10^{-7} as the grid is refined. This represents a significant improvement over the results obtained using lower NKFE.

2.6.2 Comparison of computational times.

I performed several experiments to evaluate the computational times spent by DC and Standard methods when solving similar problems to those in the previous section. The results of these experiments are depicted in Figure 2.6. To obtain them, a set of baseline error tolerances are defined, and then pairs (NKFE,PPW) close to optimal are found for each method to satisfy such thresholds. By an optimal pair I mean, the minimum values of NKFE and PPW that are needed to attain the target L^2-norm FFP relative error. Once each pair (NKFE,PPW) is found, the same simulation is performed ten times. Then, the resulting CPU times are averaged and this time average is plotted in Fig. 2.6.

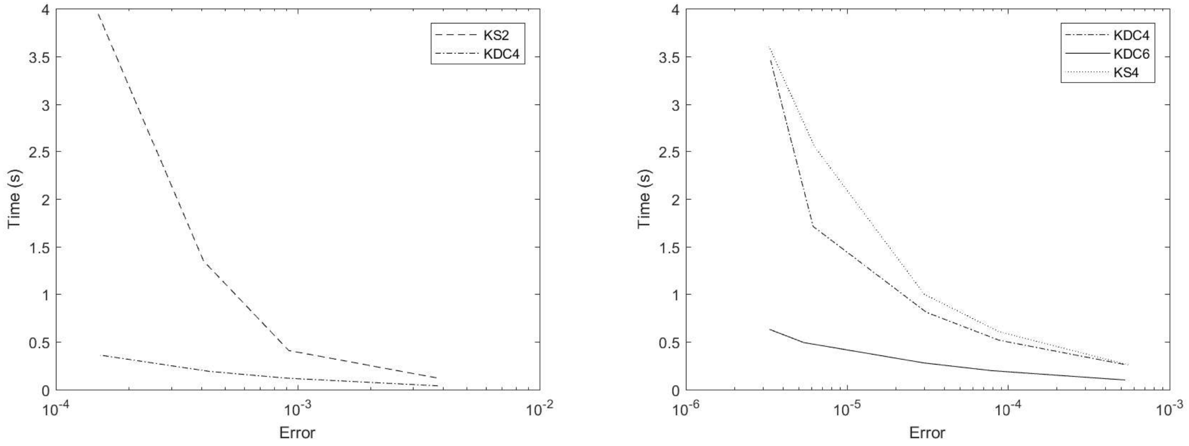

Figure 2.6: Computational times vs. L^2-norm FFP relative errors for the KS2, KDC4, KS4, and KDC6 methods.

For all simulations represented in Fig. 2.6, the relevant parameters values are $r_0 = 1$, $k = 2\pi$ and $R = 3$. Also, the pairs needed (close to optimal) to attain the FFP target errors for the different methods are depicted in Table 2.2. The curves on the left plot show that KS2 is not able to reach errors smaller than 10^{-4} during a time interval of 4 seconds, a threshold that is much earlier reached by the higher order methods, as depicted in the right plot. In fact, it is observed that the time spent by KS2 to attain an error close to 10^{-4} is about 8 times the one spent by KDC4. The limited KS2 accuracy prompted us to present two different plots with different time scales in Fig. 2.6. I noticed that KDC6 is at least three times faster than both fourth order schemes, to reach an error of 10^{-5}. The KDC4 method was second best in terms of computational time. All these experiments were performed on an Intel Core i5 laptop computer of 8 GB RAM. The codes were written and executed in MATLAB R2017b. The results are not meant to represent my methods' limiting computational speed. Instead, these are presented to demonstrate the relative speed of the different methods described.

Notice, that I needed to choose $R = 3$ to allow lower order methods to reach higher accuracies comparable to their higher order counterpart.

The sources of the time savings that are shown in Fig. 2.6 are most easily explained by examining Table 2.2. At all error levels, the DC6 scheme requires a much less refined grid and fewer Karp Expansion terms than DC4 or KS4. This leads to a smaller matrix and allows the scheme to be solved more efficiently despite the additional steps required. A similar phenomena can be seen when comparing DC4 and KS4 (especially in regards to the NKFE). The DC4 scheme have an additional efficiency advantage over the KS4 since the matrix used for solving the DC4 system is less dense than the matrix used by the KS4 method. As a note, the error values given in the table are approximations since it was not possible to find values of PPW and NKFE that would give identical errors for all three schemes. Additionally, the information displayed in Table 2.2 corresponds to the right plot in Figure 2.6, a similar table could be derived for the left plot.

FFP Tol	**KS4**		**KDC4**		**KDC6**	
error	PPW	NKFE	PPW	NKFE	PPW	NKFE
5×10^{-4}	17	8	20	8	13	2
10^{-4}	26	9	31	8	17	5
5×10^{-5}	35	9	40	8	20	6
10^{-5}	51	11	60	8	26	7
5×10^{-6}	60	11	70	8	29	8

Table 2.2: Points per wavelength and KFE number of terms needed to reach a target FFP relative error.

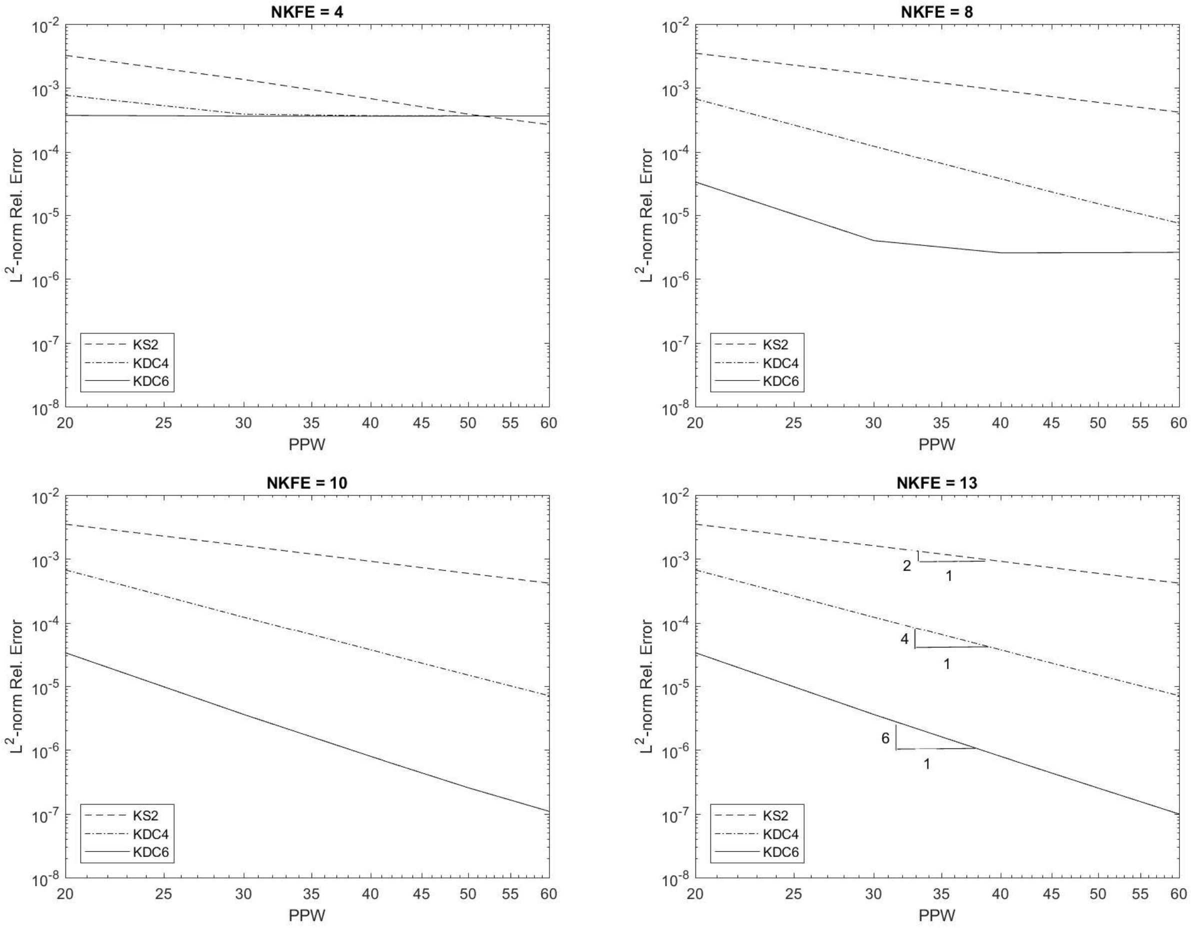

Figure 2.7: Comparison of L$_2$-norm FFP relative errors computed from KS2, KDC4 and KDC6 under Neumann BC.

2.6.3 Accuracy and convergence under Neumann BC. In this section, I compare the FFP relative errors and convergence rates of fourth- and sixth-order DC solutions for the BVP (2.6)-(2.12) under Neumann boundary conditions. For this boundary condition, the deferred correction schemes are detailed in Appendix B. In these experiments, problem parameters, PPW, and NKFE, are the same ones used for the Dirichlet type tests in Section 2.6.1. In Fig. 2.7, I compare the FFP relative errors make by the application of KS2, KDC4 and KDC6 methods for NKFE = $4, 8, 10$ and 13, while in Fig. 2.8, I exhibit the convergence rates dependence on NKFE. In both figures, the illustrated results nearly resemble the ones given in Figs. 2.3 and 2.4. Therefore, I conclude that DC accuracy and convergence rates are not affected by the type of obstacle boundary condition.

As in the Dirichlet case, the KDC4 and KDC6 methods require at least NKFE = 8 to fully reach their highest accuracy and expected convergence rates, respectively. Furthermore, for NKFE = 10 or 13, the KDC6 relative errors are two order of magnitude smaller than their KDC4 counterparts for sufficiently fine grids.

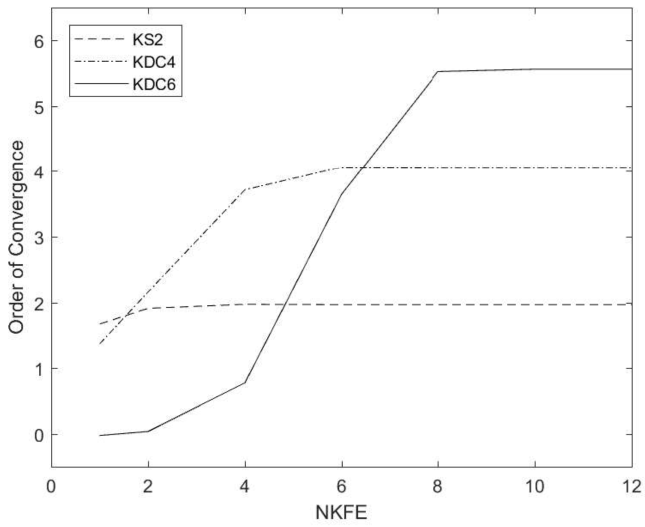

Figure 2.8: Comparison of convergence rates between the DC methods in terms of NKFE, under Neumann BC

2.7 HETEROGENEOUS MEDIA

2.7.1 The KFE-BVP for heterogeneous acoustic wave scattering . In this section, I extend the previously defined high order deferred corrections scheme to the scattering from an obstacle embedded in an unbounded acoustic heterogeneous region Ω. This is modeled by the forced Helmholtz equation for the total pressure field u_t,

$$\Delta u_t + k^2 n^2(\mathbf{x}) u_t = f(\mathbf{x}), \qquad \mathbf{x} \in \Omega \tag{2.54}$$

where $k > 0$ is the *wavenumber*, and the real-valued functions n and f are in $C^1(\Omega) \cap C(\overline{\Omega})$. The function n is called the *index of refraction*, and $1 - n^2$ and f have compact support in a bounded region $\Omega^- \subset \Omega$ that is bounded internally by the boundary of the obstacle Γ and externally by a circle of radius R (artificial boundary).

The functions n is what defines the heterogeneity of the media. Notice that $n = 1$ corresponds to the homogeneous case already discussed in the previous sections. Now, u_t consists of the scattered wave u and the incident wave u_{inc}. This means $u_t = u + u_{inc}$. Then, by inserting this decomposition of u_t into (2.54), and rearranging terms gives

$$\Delta u + k^2 n^2(\mathbf{x}) u = k^2(1 - n^2(\mathbf{x})) u_{inc} + f(\mathbf{x}) \qquad \mathbf{x} \in \Omega. \tag{2.55}$$

This equation is supplemented with the Dirichlet or Neumann boundary condition (2.7) at the obstacle boundary Γ, and the KFE absorbing boundary condition defined by the equations (2.7) -(2.12) to complete the heterogeneous KFE-BVP considered in this work. As in the homogeneous case, I specialize my study to polar coordinates and leave the extension to generalized curvilinear coordinates for later (see Appendix A). The variable coefficients of the Helmholtz equation are the main difference with respect to the homogeneous case. Therefore, at the discrete level the only changes to make, in the former treatment, are in the diagonal entries of the matrix defining the associated linear system, and in the forcing term. In fact, the main diagonal entries (2.43) of the intermediate rows ($i = 2 \dots N$) change from $-\frac{2}{\Delta r^2} - \frac{2}{r_i^2 \Delta\theta^2} + k^2$ to $-\frac{2}{\Delta r^2} - \frac{2}{r_i^2 \Delta\theta^2} + n(r_i, \theta_j) k^2$.

In the heterogeneous case, there is no exact solution for the circular obstacle. Thus, to estimate convergence rates and perform error analysis, I solved the system using a very fine grid and took that as the exact solution.

2.7.2 Numerical experiments. To analyze the accuracy and convergence of the proposed high order numerical method, I perform a set of experiments for the scattering of a time-harmonic incident plane wave $\hat{u}_{inc}(\mathbf{x}, t) = e^{-i\omega t} e^{ikx} = e^{i\omega t} u_{inc}(\mathbf{x})$ propagating in the positive direction of the x-axis from a circular obstacle. I study the effect of the degrees of heterogeneity in the medium by changing the index of refraction n inside the computational domain Ω^- . First, I consider the following smoothly varying index of refraction,

$$n_1(r) = \begin{cases} 2 & r \leq 1.25 \\ .5\cos(2\pi(r-1.25)) + 1.5 & 1.25 \leq r \leq 1.75 \\ 1 & r \geq 1.75. \end{cases} \tag{2.56}$$

Note that $n = n_1$ is gradually and smoothly decreasing from the value 2 at the obstacle boundary to the value 1 when $r = 1.75$. Therefore, starting at $r = 1.75$, the medium becomes homogeneous. The graphs for the total pressure field for $k = 2\pi$ and $R = 2, 3$ are shown in Fig. 2.9, respectively. In contrast with the homogeneous case, there is not a well-defined shadow zone. Instead, I observe oscillations in both radial and angular directions, respectively.

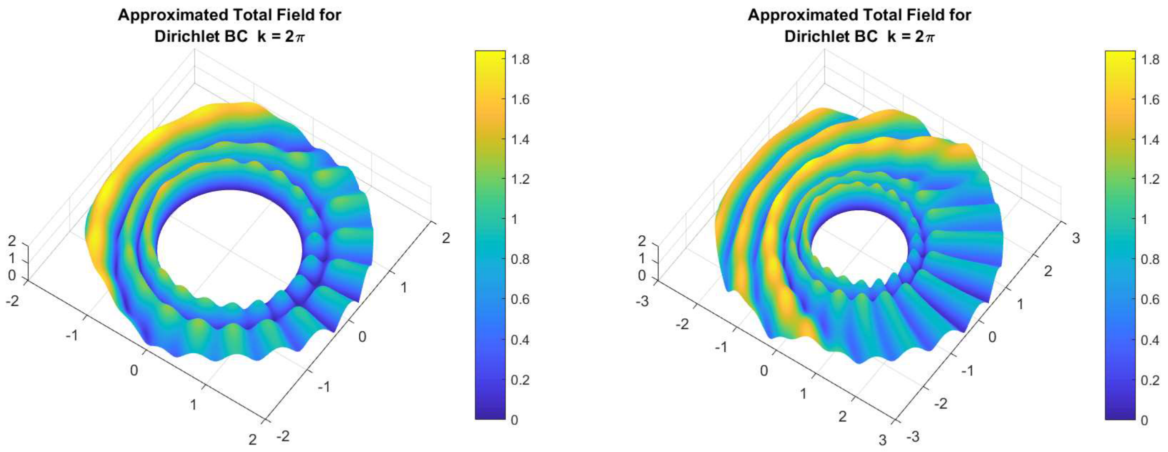

Figure 2.9: Total pressure field for the heterogeneous wave scattering problem using the function n_1 described in Equation 2.56. On the left is with $R = 2$ and on the right with $R = 3$.

For index of refraction n_1, both the 4th order and 6th order deferred corrections schemes achieved their expected level of convergence. These schemes were very robust when considering different sizes of the computational domains (values of R), different numbers of Karp expansion terms, and changes in the grid sizes. In Fig. 2.10, the 4th and 6th order convergence of the scheme can be seen. The left plot of Fig. 2.10 and its corresponding Table 2.3 show the high level of accuracy achieved by the 4th order scheme, along with its approximated order of convergence.

I also tested this high order deferred corrections method on other indices of refractions. I found

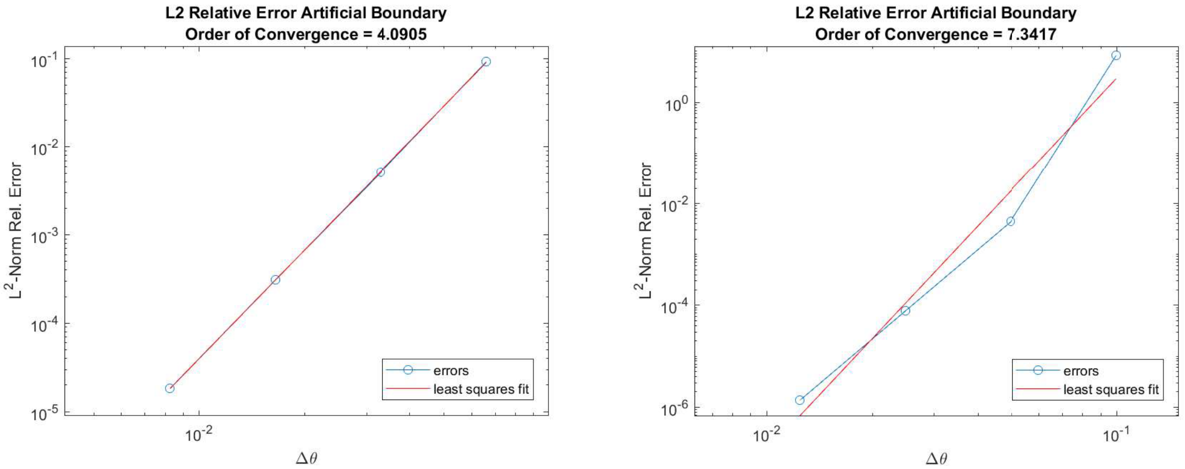

Figure 2.10: Convergence rates for 4th order (left) and 6th order (right) Deferred Correction schemes. Wavenumber varies following n_1, NKFE= 12, $R = 2$.

that other smooth functions (functions that were at least continuously differentiable) produced solutions that had similar convergence properties to those displayed by n_1. To demonstrate the robustness of this method when dealing with other smooth functions, I will include results for the following two indices of refractions:

$$n_2(r) = \begin{cases} 3 & r \leq 1.25 \\ \cos(2\pi(r - 1.25)) + 2 & 1.25 \leq r \leq 1.75 \\ 1 & r \geq 1.75, \end{cases} \tag{2.57}$$

$$n_3(r) = \begin{cases} 2 & r \leq 1.25 \\ 16r^3 - 72r^2 + 105r - 48 & 1.25 \leq r \leq 1.75 \\ 1 & r \geq 1.75. \end{cases} \tag{2.58}$$

Note that n_2 is a scaled version of n_1 while n_3 is the lowest order polynomial interpolating between the two straight lines with continuous first derivative. Plots of n_1, n_2, and n_3 are shown in Figure 2.11. As can be seen in Tables 2.3-2.5, for all of the given functions the 4th order DC method averages 4th order convergence and achieves high levels of accuracy.

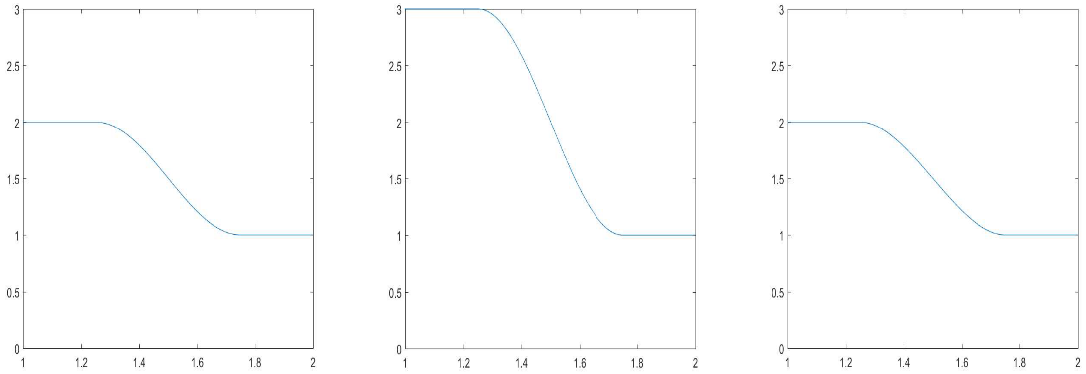

Figure 2.11: Comparison of different smoothly varying choices of n. From left to right n_1, n_2, and n_3.

$h = \Delta\theta = \Delta r$	L^2-norm Rel. Error	Observed order
0.06614	$9,07 \times 10^{-2}$	
0.03307	5.07×10^{-3}	4.16
0.01653	3.08×10^{-4}	4.03
0.00827	1.81×10^{-5}	4.09

Table 2.3: Grid spacing, L^2 Relative Error, and order of convergence for index of refraction n_1 with NKAE$=12$, $R = 2$.

$h = \Delta\theta = \Delta r$	L^2-norm Rel. Error	Observed order
0.06614	2.43×10^{-0}	
0.03307	4.26×10^{-1}	2.51
0.01653	1.42×10^{-2}	4.91
0.00827	6.24×10^{-4}	4.50

Table 2.4: Grid spacing, L^2 Relative Error, and order of convergence for index of refraction n_2 with NKAE$=12$, $R = 2$.

$h = \Delta\theta = \Delta r$	L^2-norm Rel. Error	Observed order
0.06614	8.45×10^{-2}	
0.03307	4.95×10^{-3}	4.10
0.01653	3.06×10^{-4}	4.01
0.00827	1.81×10^{-5}	4.07

Table 2.5: Grid spacing, L^2 Relative Error, and order of convergence for index of refraction n_3 with NKAE$=12$, $R = 2$.

However, when using an index of refraction with jump discontinuities, such as,

$$n_4(r) = \begin{cases} 2 & r \leq 1.25 \\ 1.5 & 1.25 < r \leq 1.75 \\ 1 & r > 1.75, \end{cases} \tag{2.59}$$

the convergence results were not quite as good as the continuous case. For instance, the numerical solution obtained from the fourth order DC method applied to the KFE-BVP with index of refraction n_4 still converged as the grid was refined, but the convergence was typically around order 2. In Fig. 2.12, the approximated total pressure field and the estimated order of convergence are illustrated for this case. This second order of convergence was typical for other non-smooth functions that I tested. I believe that this lower order of convergence, which is not consistent with the order of the numerical method, comes from a theoretical limitation of the deferred correction method. This is because of the use of high order derivatives of the solution u implicitly assumes a certain level of regularity in the solution. However, for the discontinuous index of refractions, the true solution may not exhibit the required regularity which would cause the scheme to fail to reach the expected order. It is comforting, however, that the solution still converges, despite these limitations.

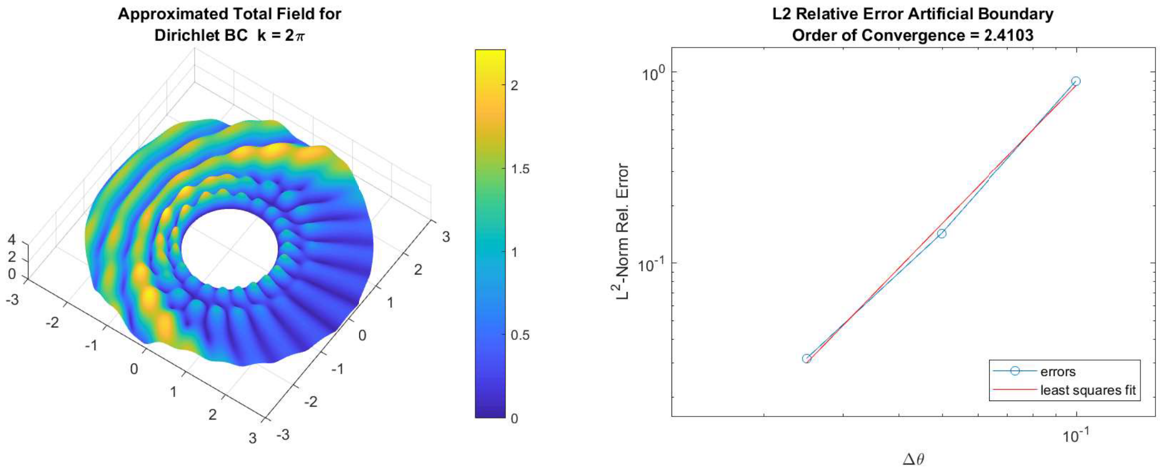

Figure 2.12: Total pressure field for the heterogeneous wave scattering problem with index of refraction n_2, NKFE$= 12$ and $R = 3$.

Additionally, my collaborators in this work are developing an alternative high order finite element (within the context of isogeometric analysis) numerical method coupled with the KFE absorbing boundary condition for this heterogeneous problem. Comparison with preliminary results, using this alternative methodology, seems to confirm that my scheme is actually converging to the true solution as my experiments suggest.

CHAPTER 3. HIGH ORDER LOCAL ABSORBING BOUNDARY CONDITIONS FOR ELASTIC WAVES IN TERMS OF FARFIELD EXPANSIONS

In this chapter, I am concerned with the scattering of time harmonic elastic waves off compact targets, which has geophysical application in exploratory seismology and seismic waves in earthquake phenomena. These problems are typically modeled by equations of elastic waves in unbounded media. Popular and efficient numerical techniques used to solve these problems include finite element and finite differences methods. These methods requires the introduction of an artificial boundary and appropriate absorbing boundary conditions (ABCs) on it. In the following, I present the construction of high order local ABCs based on farfield expansions, similar to those already defined for acoustic waves in unbounded domains [17].

3.1 CONSTRUCTION OF KARP'S FARFIELD EXPANSION ABSORBING BOUNDARY CONDITION (KFE-ABC) FOR ELASTIC WAVES

To begin, I consider an unbounded region Ω of an elastic medium. I truncate this infinite region using an artificial boundary S which is a sphere in 3D or a circle in 2D both having radius R and both containing the scattering body in its interior. This new bounded region is called Ω^-. I assume that in the exterior region $\Omega^+ = \Omega \backslash \Omega^-$ the medium is homogeneous, isotropic, and linear with constant physical properties, density ρ and Lamé constants $\mu,\ \lambda$. I will also make use of Poisson's ratio $\nu = \frac{\lambda}{2(\lambda+\mu)}$ and Young's modulus $E = \frac{\mu(3\lambda+2\mu)}{\lambda+\mu}$. I make no such assumptions for the interior region. Thus, in the exterior region, the displacement $\mathbf{U}(x, t)$ satisfies the Navier equation of linear elasticity and the Kupradze radiation conditions. I also assume that the scattered displacement $\mathbf{U}$ is time-harmonic, so $\mathbf{U}(\mathbf{x}, t) = \mathbf{u}(\mathbf{x})e^{-i\omega t}$. Then, the Navier equation in terms of the time harmonic scattered displacement $\mathbf{u}$ reduces to

$$(\lambda + 2\mu)\nabla\nabla \cdot \mathbf{u} - \nabla \times \nabla \times \mathbf{u} + \rho\omega^2\mathbf{u} = 0.$$

Also, the Kupradze radiation conditions transforms into

$$\lim_{r\to\infty} r^{(\delta-1)/2}(\partial_r \mathbf{u}^p - ik_p\mathbf{u}^p) = 0, \qquad \lim_{r\to\infty} r^{(\delta-1)/2}(\partial_r \mathbf{u}^s - k_s\mathbf{u}^s) = 0, \tag{3.1}$$

where $\mathbf{u} = \mathbf{u}^p + \mathbf{u}^s$ and the constants $k_p^2 = \omega^2 \frac{\rho}{\lambda+2\mu}$ and $k_s^2 = \omega^2 \frac{\rho}{\mu}$ are the longitudinal and transverse wavenumbers, respectively.

In this work, I will focus in the two-dimensional case. Therefore, the artificial boundary S is a circle and it is convenient to use polar coordinates (r, θ) and express $\mathbf{u}$ in terms of its radial displacement u_r and its angular displacement u_θ. Then, by using Chadwick and Trowbridge decomposition theorem [27], the scattered displacement vector $\mathbf{u}$ can be written in terms of two scalar potentials $\phi(r, \theta)$ and $\psi(r, \theta)$ as

$$\mathbf{u} = \mathbf{u}^p + \mathbf{u}^s = \nabla_{r,\theta,z}\phi + \nabla_{r,\theta,z} \times (\psi\mathbf{k}) = u_r\hat{\mathbf{r}} + u_\theta\hat{\theta}, \tag{3.2}$$

the vector $\mathbf{k}$ is the unit vector perpendicular to the xy-plane while $\hat{\mathbf{r}}$ and $\hat{\theta}$ are the local unit vectors in the radial and angular direction, respectively. Therefore,

$$u_r = \partial_r\phi + \frac{1}{r}\partial_\theta\psi \qquad u_\theta = \frac{1}{r}\partial_\theta\phi - \partial_r\psi, \tag{3.3}$$

where u_r and u_θ are the radial and angular components of the vector scattered displacement $\mathbf{u}$, respectively; and the potentials ϕ and ψ satisfy the Helmholtz equations,

$$\nabla^2\phi + k_p^2\phi = 0, \qquad \nabla^2\psi + k_s^2\psi = 0, \qquad \text{in } \Omega^-. \tag{3.4}$$

Similarly, expressions for the various elements of the stress tensor can be found [28] in terms of the potentials,

$$\sigma_{rr} = \lambda\nabla^2_{r,\theta}\phi + 2\mu\left[\partial^2_{rr}\phi - \frac{1}{r^2}\partial_\theta\psi + \frac{1}{r}\partial^2_{r\theta}\psi\right], \tag{3.5}$$

$$\sigma_{r\theta} = 2\mu\left[\frac{1}{r}\partial^2_{\theta r}\phi - \frac{1}{r^2}\partial_\theta\phi\right] + \mu\left[\frac{1}{r^2}\partial^2_{\theta\theta}\psi + \frac{1}{r}\partial_r\psi - \partial^2_{rr}\psi\right]. \tag{3.6}$$

Furthermore, the Kupradze radiation condition (3.1) implies that the scalar potentials ϕ and ψ satisfy the Sommerfeld radiation condition at infinity, i.e.,

$$\lim_{r\to\infty} r^{(\delta-1)/2}\left(\partial_r\phi - ik_p\phi\right) = 0, \quad \lim_{r\to\infty} r^{(\delta-1)/2}\left(\partial_r\psi - ik_s\psi\right) = 0. \tag{3.7}$$

As a consequence, ϕ and ψ are outgoing solutions of the two-dimensional Helmholtz equations (3.4). Therefore according to Karp's theorem [23], they can be written as the following convergent expansions in the region Ω^+, located in the exterior to the circle of radius $r = R$,

$$\phi(r,\theta) = \mathcal{K}^p(r,\theta) \equiv H_0(k_pr)\sum_{l=0}^{\infty}\frac{F_l^p(\theta)}{(k_pr)^l} + H_1(k_pr)\sum_{l=0}^{\infty}\frac{G_l^p(\theta)}{(k_pr)^l}, \qquad \text{for } r > R, \tag{3.8}$$

$$\psi(r,\theta) = \mathcal{K}^s(r,\theta) \equiv H_0(k_sr)\sum_{l=0}^{\infty}\frac{F_l^s(\theta)}{(k_sr)^l} + H_1(k_sr)\sum_{l=0}^{\infty}\frac{G_l^s(\theta)}{(k_sr)^l}, \qquad \text{for } r > R, \tag{3.9}$$

and the coefficient angular functions satisfy the following recurrence formulas,

$$2lG_l^{p,s}(\theta) = (l-1)^2F_{l-1}^{p,s}(\theta) + d_\theta^2F_{l-1}^{p,s}(\theta), \qquad 2lF_l^{p,s}(\theta) = -l^2G_{l-1}^{p,s}(\theta) - d_\theta^2G_{l-1}^{p,s}(\theta), \tag{3.10}$$

for $l = 1, 2, \ldots$.

Now, I proceed to the construction of the KFE-ABC of the elastic waves at the artificial boundary $r = R$. This construction is similar to the one followed for the acoustic waves. Since the potentials satisfy the Helmholtz equation, I expect them to be continuous at the artificial boundary, $r = R$. As a result, I arrive to my first two equations defining the KFE-ABC,

$$\phi(R,\theta) = \mathcal{K}^p_{L-1}(R,\theta) \equiv H_0(k_pR)\sum_{l=0}^{L-1}\frac{F^p_l(\theta)}{(k_pR)^l} + H_1(k_pR)\sum_{l=0}^{L-1}\frac{G^p_l(\theta)}{(k_pR)^l}, \tag{3.11}$$

$$\psi(R,\theta) = \mathcal{K}^s_{L-1}(R,\theta) \equiv H_0(k_sR)\sum_{l=0}^{L-1}\frac{F^s_l(\theta)}{(k_sR)^l} + H_1(k_sR)\sum_{l=0}^{L-1}\frac{G^s_l(\theta)}{(k_sR)^l} \tag{3.12}$$

Notice that for computational reasons, I have used a truncated version of Karp's expansions in the above conditions, denoted by $\mathcal{K}^p_{L-1}$ and $\mathcal{K}^s_{L-1}$. Thus, the numerical solution obtained by applying these conditions should improve its accuracy by increasing the number of terms L in the Karp's expansions.

Next, I require continuity of the scattered displacement components at the artificial boundary $r = R$, which leads to

$$u_r(R,\theta) = \partial_r\phi(R,\theta) + \frac{1}{R}\partial_\theta\psi(R,\theta) = \partial_r\mathcal{K}^p_{L-1}(R,\theta) + \frac{1}{R}\partial_\theta\mathcal{K}^s_{L-1}(R,\theta) \tag{3.13}$$

$$u_\theta(R,\theta) = \frac{1}{R}\partial_\theta\phi(R,\theta) - \partial_r\psi(R,\theta) = \frac{1}{R}\partial_\theta\mathcal{K}^p_{L-1}(R,\theta) - \partial_r\mathcal{K}^s_{L-1}(R,\theta). \tag{3.14}$$

In addition, I require the continuity of the two components of the stress tensor in the radial direction. Thus,

$$\begin{aligned}\sigma_{rr}(R,\theta) = \lambda\nabla^2_{r,\theta}\phi(R,\theta) + 2\mu\left[\partial^2_r\phi - \frac{1}{R^2}\partial_\theta\psi + \frac{1}{R}\partial^2_{r\theta}\psi\right](R,\theta) = \lambda\nabla^2_{r,\theta}\mathcal{K}^p_{L-1}(R,\theta) + \\ 2\mu\left[\partial^2_r\mathcal{K}^p_{L-1} - \frac{1}{R^2}\partial_\theta\mathcal{K}^s_{L-1} + \frac{1}{R}\partial^2_{r\theta}\mathcal{K}^s_{L-1}\right](R,\theta),\end{aligned} \tag{3.15}$$

$$\begin{aligned}\sigma_{r\theta}(R,\theta) = 2\mu\left[\frac{1}{R}\partial^2_{r\theta}\phi(R,\theta) + \frac{1}{R^2}\partial_\theta\phi\right](R,\theta) + \mu\left[\frac{1}{R^2}\partial^2_\theta\psi + \frac{1}{R}\partial_r\psi - \partial^2_r\psi\right](R,\theta) = \\ 2\mu\left[\frac{1}{R}\partial^2_{r\theta}\mathcal{K}^p_{L-1} + \frac{1}{R^2}\partial_\theta\mathcal{K}^p_{L-1}\right](R,\theta) + \mu\left[\frac{1}{R^2}\partial^2_\theta\mathcal{K}^s_{L-1} + \frac{1}{R}\partial_r\mathcal{K}^s_{L-1} - \partial^2_r\mathcal{K}^s_{L-1}\right](R,\theta).\end{aligned} \tag{3.16}$$

Finally, I have the recursion formulas to determine the angular functions of Karp's expansions.

They are given by

$$2lG_l^p(\theta) = (l-1)^2 F_{l-1}^p(\theta) + d_\theta^2 F_{l-1}^p(\theta), \qquad \text{for } l = 1, 2, \ldots L-1 \tag{3.17}$$

$$2lF_l^p(\theta) = -l^2 G_{l-1}^p(\theta) - d_\theta^2 G_{l-1}^p(\theta), \qquad \text{for } l = 1, 2, \ldots L-1 \tag{3.18}$$

$$2lG_l^s(\theta) = (l-1)^2 F_{l-1}^s(\theta) + d_\theta^2 F_{l-1}^s(\theta), \qquad \text{for } l = 1, 2, \ldots L-1 \tag{3.19}$$

$$2lF_l^s(\theta) = -l^2 G_{l-1}^s(\theta) - d_\theta^2 G_{l-1}^s(\theta), \qquad \text{for } l = 1, 2, \ldots L-1. \tag{3.20}$$

The set of equations (3.11)-(3.20) constitute my novel KFE-ABC for elastic waves.

The reason why all these equations are needed to define the KFE-ABC is explained by counting the unknowns and the number of equations constituting it. In fact, in the six equations (3.11)-(3.16) are six unknowns given by ϕ, ψ, F_0^p, G_0^p, F_0^s, and G_0^s. In addition, for every term added to the Karp series expansion (3.11) there are an additional four unknowns given by F_l^p, G_l^p, F_l^s, G_l^s. In total, this gives $6 + 4 \cdot (L-1)$ unknonwns for $l = L-1$. This is the same as the number of equations in (3.11)-(3.20).

3.2 ELASTIC SCATTERING KFE BOUNDARY VALUE PROBLEM (KFE-BVP)

Now, I consider the scattering of an incident plane wave from a circular obstacle of radius $r = r_0$. This incident wave is represented in terms of the scalar potentials by

$$\phi(r_0, \theta) = \phi_{inc}(r_0, \theta) = e^{ikx} = e^{ikr\cos\theta}, \qquad \text{and} \quad \psi(r_0, \theta) = \psi_{inc}(r_0, \theta) = 0, \tag{3.21}$$

As described earlier, for a complete formulation of the elastic scattering problem, boundary conditions at the obstacle boundary $r = r_0$ need to be included. I have chosen to address two types of boundary conditions in this work. The first is a soft obstacle boundary which corresponds to no total stress at the obstacle boundary. Since the total displacement $\mathbf{u}_T = \mathbf{u}_{inc} + \mathbf{u}$ and the differential operators defining the stress components are linear, this condition is equivalent to

$$\sigma_{rr}(r_0,\theta) = -(\sigma_{inc})_{rr}(r_0,\theta) \qquad \text{and} \quad \sigma_{r\theta}(r_0,\theta) = -(\sigma_{inc})_{r\theta}(r_0,\theta), \tag{3.22}$$

where σ_{inc} represents the stress tensor due to the incident wave, as stated in [28]. Representing these radial stresses in terms of the potentials gives

$$\begin{aligned} -\lambda k_p^2 \phi(r_0,\theta) + 2\mu \left[\partial_r^2 \phi - \frac{1}{r^2}\partial_\theta \psi + \frac{1}{r}\partial_{r\theta}^2 \psi\right](r_0,\theta) & \qquad (3.23) \\ = \left[\lambda k_p^2 - 2\mu(ik_p\cos(\theta))^2\right]\phi_{inc}(r_0,\theta) & \\ 2\mu\left[\frac{1}{r}\partial_{r\theta}^2\phi(r_0,\theta) + \frac{1}{r^2}\partial_\theta\phi\right](r_0,\theta) + \mu\left[\frac{1}{r^2}\partial_\theta^2\psi + \frac{1}{r}\partial_r\psi - \partial_r^2\psi\right](r_0,\theta) = & \qquad (3.24) \\ = 2\mu(ik_p)^2\cos(\theta)\sin(\theta)\phi_{inc}(r_0,\theta). & \end{aligned}$$

The second is a hard obstacle boundary which corresponds to zero total displacement at the obstacle boundary, which is equivalent to

$$u_r(r_0,\theta) = -(u_{inc})_r(r_0,\theta) \qquad \text{and} \quad u_\theta(r_0,\theta) = -(u_{inc})_\theta(r_0,\theta), \tag{3.25}$$

which, in terms of the scalar potentials, reduces to

$$u_r(r_0,\theta) = \partial_r\phi(r_0,\theta) + \frac{1}{r_0}\partial_\theta\psi(r_0,\theta) = -ik_p\cos(\theta)\phi_{inc}(r_0,\theta) \tag{3.26}$$

$$u_\theta(r_0,\theta) = \frac{1}{r_0}\partial_\theta\phi(r_0,\theta) - \partial_r\phi(r_0,\theta) = ik_p\sin(\theta)\phi_{inc}(r_0,\theta). \tag{3.27}$$

Summarizing, the BVP of the elastic scattering of the incident wave (3.21) from an obstacle with a circular boundary in terms of the scalar potentials ϕ and ψ is given by the following equations:

The Helmholtz quations at the interior;

$$\nabla^2\phi + k_p^2\phi = 0, \qquad \nabla^2\psi + k_s^2\psi = 0, \qquad \text{in } \Omega^-,$$

the scatterer boundary conditions (soft);

$$\begin{aligned}
-\lambda k_p^2\phi(r_0,\theta) + 2\mu\left[\partial_r^2\phi - \frac{1}{r^2}\partial_\theta\psi + \frac{1}{r}\partial_{r\theta}^2\psi\right](r_0,\theta)& \\
&= \left[\lambda k_p^2 - 2\mu(ik_p\cos(\theta))^2\right]\phi_{inc}(r_0,\theta), \\
2\mu\left[\frac{1}{r}\partial_{r\theta}^2\phi(r_0,\theta) + \frac{1}{r^2}\partial_\theta\phi\right](r_0,\theta) + \mu\left[\frac{1}{r^2}\partial_\theta^2\psi + \frac{1}{r}\partial_r\psi - \partial_r^2\psi\right](r_0,\theta)& \\
&= 2\mu(ik_p)^2\cos(\theta)\sin(\theta)\phi_{inc}(r_0,\theta),
\end{aligned}$$

or scatterer boundary conditions (hard);

$$\begin{aligned}
u_r(r_0,\theta) &= \partial_r\phi(r_0,\theta) + \frac{1}{r_0}\partial_\theta\psi(r_0,\theta) = -ik_p\cos(\theta)\phi_{inc}(r_0,\theta), \\
u_\theta(r_0,\theta) &= \frac{1}{r_0}\partial_\theta\phi(r_0,\theta) - \partial_r\phi(r_0,\theta) = ik_p\sin(\theta)\phi_{inc}(r_0,\theta),
\end{aligned}$$

the continuity of the scalar potentials at $r = R$;

$$\phi(R,\theta) = \mathcal{K}_{L-1}^p(R,\theta),$$

$$\psi(R,\theta) = \mathcal{K}_{L-1}^s(R,\theta),$$

the continuity of the displacement components at $r = R$;

$$\begin{aligned}
u_r(R,\theta) &= \partial_r\phi(R,\theta) + \frac{1}{R}\partial_\theta\psi(R,\theta) = \partial_r\mathcal{K}_{L-1}^p(R,\theta) + \frac{1}{R}\partial_\theta\mathcal{K}_{L-1}^s(R,\theta), \\
u_\theta(R,\theta) &= \frac{1}{R}\partial_\theta\phi(R,\theta) - \partial_r\psi(R,\theta) = \frac{1}{R}\partial_\theta\mathcal{K}_{L-1}^p(R,\theta) - \partial_r\mathcal{K}_{L-1}^s(R,\theta),
\end{aligned}$$

the continuity of the stress components in the radial direction at $r = R$;

$$\sigma_{rr}(R,\theta) = \lambda\nabla^2_{r,\theta}\phi(R,\theta) + 2\mu\left[\partial^2_r\phi - \frac{1}{R^2}\partial_\theta\psi + \frac{1}{R}\partial^2_{r\theta}\psi\right](R,\theta)$$

$$= \lambda\nabla^2_{r,\theta}\mathcal{K}^p_{L-1}(R,\theta) + 2\mu\left[\partial^2_r\mathcal{K}^p_{L-1} - \frac{1}{R^2}\partial_\theta\mathcal{K}^s_{L-1} + \frac{1}{R}\partial^2_{r\theta}\mathcal{K}^s_{L-1}\right](R,\theta),$$

$$\sigma_{r\theta}(R,\theta) = 2\mu\left[\frac{1}{R}\partial^2_{r\theta}\phi(R,\theta) + \frac{1}{R^2}\partial_\theta\phi\right](R,\theta) +$$

$$\mu\left[\frac{1}{R^2}\partial^2_\theta\psi + \frac{1}{R}\partial_r\psi - \partial^2_r\psi\right](R,\theta) = 2\mu\left[\frac{1}{R}\partial^2_{r\theta}\mathcal{K}^p_{L-1} + \frac{1}{R^2}\partial_\theta\mathcal{K}^p_{L-1}\right](R,\theta)$$

$$+\,\mu\left[\frac{1}{R^2}\partial^2_\theta\mathcal{K}^s_{L-1} + \frac{1}{R}\partial_r\mathcal{K}^s_{L-1} - \partial^2_r\mathcal{K}^s_{L-1}\right](R,\theta),$$

and the recursion formulas for the angular coefficients;

$$2lG^p_l(\theta) = (l-1)^2F^p_{l-1}(\theta) + d^2_\theta F^p_{l-1}(\theta), \qquad \text{for } l = 1,2,\dots L-1$$

$$2lF^p_l(\theta) = -l^2G^p_{l-1}(\theta) - d^2_\theta G^p_{l-1}(\theta), \qquad \text{for } l = 1,2,\dots L-1$$

$$2lG^s_l(\theta) = (l-1)^2F^s_{l-1}(\theta) + d^2_\theta F^s_{l-1}(\theta), \qquad \text{for } l = 1,2,\dots L-1$$

$$2lF^s_l(\theta) = -l^2G^s_{l-1}(\theta) - d^2_\theta G^s_{l-1}(\theta), \qquad \text{for } l = 1,2,\dots L-1.$$

3.3 EQUIVALENT KFE ABSORBING BOUNDARY CONDITIONS FOR ELASTIC WAVES

In this Section, I derive simplified and equivalent conditions to (3.13)-(3.16) that are very convenient for numerical computation. Their convenience comes from the reduction in the number of derivatives to be approximated. In fact,

Theorem 3.1. *Assuming that (3.11) and (3.12) hold, then the conditions*

$$\partial_r\phi(R,\theta) = \partial_r\mathcal{K}^p_{L-1}(R,\theta) \tag{3.28}$$

$$\partial_r\psi(R,\theta) = \partial_r\mathcal{K}^s_{L-1}(R,\theta) \tag{3.29}$$

are equivalent to (3.13) and (3.14).

Proof. By (3.11), $\phi(R,\theta) = \mathcal{K}^p_{L-1}(R,\theta)$ for all θ. Thus, $\partial_\theta\phi(R,\theta) = \partial_\theta\mathcal{K}^p_{L-1}(R,\theta)$. This transforms (3.13) into

$$\partial_r\phi(R,\theta) + \frac{1}{R}\partial_\theta\psi(R,\theta) = \partial_r\mathcal{K}^p_{L-1}(R,\theta) + \frac{1}{R}\partial_\theta\psi(R,\theta)$$

and (3.14) into

$$\frac{1}{R}\partial_\theta\phi(R,\theta) - \partial_r\psi(R,\theta) = \frac{1}{R}\partial_\theta\phi(R,\theta) - \partial_r\mathcal{K}^s_{L-1}(R,\theta).$$

Subtracting $\frac{1}{R}\partial_\theta\psi(R,\theta)$ from both sides of the first equation and $\frac{1}{R}\partial_\theta\phi(R,\theta)$ from both sides of the second equation gives (3.28) and (3.29), respectively. □

Theorem 3.2. *Assume that (3.28) and (3.29) hold for all θ. In addition, assume that the conditions of Theorem 3.1 also hold, then*

$$\partial_r^2\phi(R,\theta) = \partial_r^2\mathcal{K}^p_{L-1}(R,\theta) \tag{3.30}$$

$$\partial_r^2\psi(R,\theta) = \partial_r^2\mathcal{K}^s_{L-1}(R,\theta) \tag{3.31}$$

are equivalent to (3.15) and (3.16).

Proof. By the proof of Theorem 3.1, $\partial_\theta\phi(R,\theta) = \partial_\theta\mathcal{K}^p_{L-1}(R,\theta)$. Since this is true for all θ, it must be that $\partial_\theta^2\phi(R,\theta) = \partial_\theta^2\mathcal{K}^p_{L-1}(R,\theta)$ as well. Also by the first assumption, $\partial_\theta(\partial_r\phi)(R,\theta) = \partial_\theta(\partial_r\mathcal{K}^p_{L-1})(R,\theta)$ and $\partial_\theta(\partial_r\psi)(R,\theta) = \partial_\theta(\partial_r\mathcal{K}^s_{L-1})(R,\theta)$. These results imply that (3.15) can be rewritten as

$$\lambda\left(\partial_r^2\phi + \frac{1}{R}\partial_r\phi + \frac{1}{r^2}\partial_\theta^2\phi\right)(R,\theta) + 2\mu\left[\partial_r^2\phi - \frac{1}{R^2}\partial_\theta\psi + \frac{1}{R}\partial_\theta\partial_r\psi\right](R,\theta) =$$
$$\lambda\left(\partial_r^2\mathcal{K}^p_{L-1} + \frac{1}{R}\partial_r\phi + \frac{1}{r^2}\partial_\theta^2\phi\right)(R,\theta) + 2\mu\left[\partial_r^2\mathcal{K}^p_{L-1} - \frac{1}{R^2}\partial_\theta\psi + \frac{1}{R}\partial_\theta\partial_r\psi\right](R,\theta).$$

After cancellation of common terms in both sides results $(\lambda+2\mu)\partial_r^2\phi(R,\theta) = (\lambda+2\mu)\partial_r^2\mathcal{K}^p_{L-1}(R,\theta)$.

Dividing both sides of that equation by $\lambda + 2\mu$ gives (3.30). Similarly, (3.14) can be rewritten as

$$
\begin{aligned}
&2\mu\left[\frac{1}{R}\partial_\theta\partial_r\phi + \frac{1}{R^2}\partial_\theta\phi\right](R,\theta) + \mu\left[\frac{1}{R^2}\partial_\theta^2\psi + \frac{1}{R}\partial_r\psi - \partial_r^2\psi\right](R,\theta) = \\
&2\mu\left[\frac{1}{R}\partial_\theta\partial_r\phi + \frac{1}{R^2}\partial_\theta\phi\right](R,\theta) + \mu\left[\frac{1}{R^2}\partial_\theta^2\psi + \frac{1}{R}\partial_r\psi - \partial_r^2\mathcal{K}_{L-1}^s\right](R,\theta).
\end{aligned}
$$

Subtracting the first four terms from both sides of the equation gives $-\mu\partial_r^2\psi(R,\theta) = -\mu\partial_r^2\mathcal{K}_{L-1}^s(R,\theta)$. Dividing both sides of that equation by $-\mu$ gives (3.31). $\square$

3.4 NUMERICAL SCHEME FOR THE KFE-BVP OF ELASTIC SCATTERING

The bounded KFE-BVP that I have proposed to obtain an approximation to the solution of the elastic scattering from a single obstacle is given by (3.4) and (3.11)-(3.20) with an additional Dirichlet (3.26)-(3.27) or Neumann (3.23)-(3.24) boundary condition at the obstacle boundary. In this section I develop a second order finite difference numerical method to obtain an approximate solution to this BVP. Throughout this section, I will use the following equations to simplify writing the Karp expansion,

$$
J_h^p = \frac{H_0(k_pR)}{(k_pR)^h},\ K_h^p = \frac{H_1(k_pR)}{(k_pR)^h}
$$

$$
J_h^s = \frac{H_0(k_sR)}{(k_sR)^h},\ K_h^s = \frac{H_1(k_sR)}{(k_sR)^h}.
$$

Just as in Section 2.3.1, I cover the domain Ω^- with a polar grid with constant radial and angular steps Δr and $\Delta\theta$, respectively. The number of grid points in the radial and angular directions is $N, m > 1$, respectively. For a given grid point (r_i, θ_j), the discrete value of the scattered field is denoted by $u_{i,j} = u(r_i, \theta_j)$. Notice that the pairs (r_i, θ_1) and (r_i, θ_{m+1}) represent the same physical point due to periodicity in the angular direction, thus $u_{i,1} = u_{i,m+1}$ for $i \leq N$. Thus, the grid supports $N \times m$ wavefield evaluations.

The KFE-BVP leads to a well-posed linear system after discretization. For this, I will consider the unknowns to be computed along with the corresponding set of equations. In the interior, $\phi_{i,j}$ and $\psi_{i,j}$ will be computed where $i = 1, \ldots, N-1$ and $j = 1, \ldots, m$ for a total of $2 \cdot (N-1) \cdot m$

unknowns. Near the obstacle boundary, discretizations of derivatives cause the introduction of an additional $2 \cdot m$ points at $\phi_{0,j}$ and $\psi_{0,j}$. These points are known as ghost points since they do not correspond to physical points outside of the scattering body but are instead used to aid in computation. In addition, I will truncate the two Karp Expansion series to $L-1$. This means I have $F_l^p(\theta_j)$, $G_l^p(\theta_j)$, $F_l^s(\theta_j)$, and $G_l^s(\theta_j)$ for $j = 1, \ldots, m$ and $l = 0, \ldots, L-1$. This gives an additional $4 \cdot L \cdot m$ unknowns. Finally, $2 \cdot m$ more unknowns at $\phi_{N+1,j}$ and $\psi_{N+1,j}$ will be added to aid in the computation of points near the absorbing boundary. Once again, these are ghost points since they correspond to points outside of Ω^-. The first set of $2 \cdot m$ equations comes from the boundary conditions (either hard or soft obstacle, to be discussed later). For the second set of equations, I consider the Helmholtz equations centered at i, j for $i = 1, \ldots, N$, this introduces $2 \cdot N \cdot m$ equations. Note that any time the variables $\phi_{N,j}$ or $\psi_{N,j}$ appear, they will be replaced with the appropriate Karp expansion using (3.11) and (3.12). I then use four interface type conditions (3.13)-(3.15) to obtain equations for the next $4 \cdot m$ unknowns. The final set of $4 \cdot (L-1) \cdot m$ unknowns are taken care of by (3.17)-(3.20).

The following equations are the discretized version of equations (3.4), (3.11)-(3.20). Throughout this section, I will refer to “blocks” of the matrix relating to the final numerical scheme. Each “block” refers to a section of m contiguous rows that correspond to a single angular slice.

The first set of $2 \cdot m$ equations take up the first two blocks of the matrix and correspond to the equations describing the obstacle boundary. In the case of the soft obstacle boundary equations (3.23)-(3.24) become

$$\begin{aligned}(-\lambda k_p^2 - \frac{4\mu}{\Delta r^2})\phi_{1,j} + \frac{2\mu}{\Delta r^2}(\phi_{0,j} + \phi_{2,j}) - \frac{\mu}{r_1^2 \Delta\theta}(\psi_{1,j+1} - \psi_{1,j-1}) \\ + \frac{\mu}{2 r_1 \Delta r \Delta\theta}(\psi_{2,j+1} - \psi_{0,j+1} - \psi_{2,j-1} + \psi_{0,j-1}) \\ = \left[\lambda k_p^2 - 2\mu(i k_p \cos(\theta_j))^2\right](\phi_{inc})_{1,j}\end{aligned} \tag{3.32}$$

$$\frac{\mu}{2r_1\Delta r\Delta\theta}(\phi_{2,j+1}-\phi_{0,j+1}-\phi_{2,j-1}+\phi_{0,j-1})-\frac{\mu}{r_1^2\Delta\theta}(\phi_{1,j+1}-\phi_{1,j-1}) \tag{3.33}$$
$$+(-\frac{2\mu}{r_1^2\Delta\theta^2}+\frac{2\mu}{\Delta r^2})\psi_{1,j}+(\frac{\mu}{2r_1\Delta r}-\frac{\mu}{\Delta r^2})\psi_{2,j}$$
$$+(-\frac{\mu}{2r_1\Delta r}-\frac{\mu}{\Delta r^2})\psi_{0,j}+\frac{\mu}{r_1^2\Delta\theta^2}(\psi_{1,j+1}+\psi_{1,j-1})$$
$$=2\mu(ik_p)^2\cos(\theta_j)\sin(\theta_j)(\phi_{inc})_{1,j}.$$

Note that $\phi_{0,j}$ and $\psi_{0,j}$ are ghost points whose computation is taken care of by the inclusion of the Helmholtz equation (3.4) at $i = 1$. In the case of the hard obstacle boundary equations (3.26)-(3.27) become

$$\frac{\phi_{2,j}-\phi_{0,j}}{2\Delta r}+\frac{\psi_{2,j}-\psi_{0,j}}{2r_1\Delta\theta}=-ik_p\cos(\theta_j)(\phi_{inc})_{1,j} \tag{3.34}$$
$$\frac{\phi_{2,j}-\phi_{0,j}}{2r_1\Delta\theta}-\frac{\psi_{2,j}-\psi_{0,j}}{2\Delta r}=ik_p\sin(\theta_j)(\phi_{inc})_{1,j}. \tag{3.35}$$

The $2\cdot(N-2)$ blocks corresponding to the interior points (r_i,θ_j) ($i = 2,\dots N-2$, $j = 1,\dots m$), as well as the points at the obstacle boundary at $i = 1$, follow. Their corresponding equations are obtained from the discretization of the Helmholtz equation.

$$\alpha_i^+\phi_{i+1,j}+\alpha_i^-\phi_{i-1,j}+\alpha_i^p\phi_{i,j}+\beta_i\phi_{i,j+1}+\beta_i\phi_{i,j-1}=0, \tag{3.36}$$
$$\alpha_i^+\psi_{i+1,j}+\alpha_i^-\psi_{i-1,j}+\alpha_i^s\psi_{i,j}+\beta_i\psi_{i,j+1}+\beta_i\psi_{i,j-1}=0, \tag{3.37}$$
$$\alpha_i^+=\tfrac{1}{\Delta r^2}+\tfrac{1}{(2\Delta r)r_i},\qquad \alpha_i^-=\tfrac{1}{\Delta r^2}-\tfrac{1}{(2\Delta r)r_i},$$
$$\alpha_i^p=k_p^2-\tfrac{2}{\Delta r^2}-\tfrac{2}{\Delta\theta^2 r_i^2},\qquad \beta_i=\tfrac{1}{\Delta\theta^2 r_i^2},$$
$$\alpha_i^s=k_s^2-\tfrac{2}{\Delta r^2}-\tfrac{2}{\Delta\theta^2 r_i^2}.$$

The next two blocks correspond to the interior points (r_i,θ_j) ($i = N-1$ $j = 1,\dots m$) where the replacement of $\phi_{N,j}$ and $\psi_{N,j}$ using (3.11) and (3.12) causes the Helmholtz equation to become

$$\alpha^{+}_{N-1}\left(\sum_{h=0}^{L-1} J^p_h F^p_{h,j} + \sum_{h=0}^{L-1} K^p_h G^p_{h,j}\right) + \alpha^{-}_{N-1}\phi_{N-2,j} + \alpha^{p}_{N-1}\phi_{N-1,j} \tag{3.38}$$

$$+ \beta_{N-1}\phi_{N-1,j+1} + \beta_{N-1}\phi_{N-1,j-1} = 0,$$

$$\alpha^{+}_{N-1}\left(\sum_{h=0}^{L-1} J^s_h F^s_{h,j} + \sum_{h=0}^{L-1} K^s_h G^s_{h,j}\right) + \alpha^{-}_{N-1}\psi_{N-2,j} + \alpha^{s}_{N-1}\psi_{N-1,j} \tag{3.39}$$

$$+ \beta_{N-1}\psi_{N-1,j+1} + \beta_{N-1}\psi_{N-1,j-1} = 0.$$

At the artificial boundary (r_i, θ_j) $(i = N \ j = 1, \ldots m)$, a similar replacement transforms the Helmholtz equation into

$$\alpha^{+}_{N}\phi_{N+1,j} + \alpha^{-}_{N}\phi_{N-1,j} + \alpha^{p}_{N}\left(\sum_{h=0}^{L-1} J^p_h F^p_{h,j} + \sum_{h=0}^{L-1} K^p_h G^p_{h,j}\right) \tag{3.40}$$

$$+ \beta_N\left(\sum_{h=0}^{L-1} J^p_h F^p_{h,j+1} + \sum_{h=0}^{L-1} K^p_h G^p_{h,j+1}\right) + \beta_N\left(\sum_{h=0}^{L-1} J^p_h F^p_{h,j-1} + \sum_{h=0}^{L-1} K^p_h G^p_{h,j-1}\right) = 0$$

$$\alpha^{+}_{N}\psi_{N+1,j} + \alpha^{-}_{N}\psi_{N-1,j} + \alpha^{s}_{N}\left(\sum_{h=0}^{L-1} J^s_h F^s_{h,j} + \sum_{h=0}^{L-1} K^s_h G^s_{h,j}\right) \tag{3.41}$$

$$+ \beta_N\left(\sum_{h=0}^{L-1} J^s_h F^s_{h,j+1} + \sum_{h=0}^{L-1} K^s_h G^s_{h,j+1}\right) + \beta_N\left(\sum_{h=0}^{L-1} J^s_h F^s_{h,j-1} + \sum_{h=0}^{L-1} K^s_h G^s_{h,j-1}\right) = 0.$$

I now define some constants that will be useful in later equations:

$$A^p_h = -\frac{k_p H_1}{(k_p R)^h} - \frac{k_p h H_0}{(k_p R)^{h+1}}$$

$$B^p_h = -\frac{k_p (h+1) H_1}{(k_p R)^{h+1}} + \frac{k_p H_0}{(k_p R)^h}$$

$$A^s_h = -\frac{k_s H_1}{(k_s R)^h} - \frac{k_s h H_0}{(k_s R)^{h+1}}$$

$$B^s_h = -\frac{k_s (h+1) H_1}{(k_s R)^{h+1}} + \frac{k_s H_0}{(k_s R)^h}$$

$$C_h^p = -\frac{k_p^2 H_0}{(k_p R)^h} + \frac{k_p^2(2h+1)H_1}{(k_p R)^{h+1}} + \frac{k_p^2 h(h+1)H_0}{(k_p R)^{h+2}}$$

$$D_h^p = \frac{k_p^2(2h+1)H_0}{(k_p R)^{h+1}} - \frac{k_p^2 H_1}{(k_p R)^h} + \frac{k_p^2(h+1)(h+2)H_1}{(k_p R)^{h+2}}$$

$$C_h^s = -\frac{k_s^2 H_0}{(k_s R)^h} + \frac{k_s^2(2h+1)H_1}{(k_s R)^{h+1}} + \frac{k_s^2 h(h+1)H_0}{(k_s R)^{h+2}}$$

$$D_h^s = \frac{k_s^2(2h+1)H_0}{(k_s R)^{h+1}} - \frac{k_s^2 H_1}{(k_s R)^h} + \frac{k_s^2(h+1)(h+2)H_1}{(k_s R)^{h+2}}.$$

Note thtat A and B are related to the first partial derivative with respect to r of the coefficients of the Karp expansion terms while C and D are related to the second partial derivative.

The next two blocks are made up of the first interface conditions

$$\frac{\phi_{N+1,j} - \phi_{N-1,j}}{2\Delta r} - \sum_{h=0}^{L-1} A_h^p F_{h,j}^p - \sum_{h=0}^{L-1} B_h^p G_{h,j}^p = 0$$

$$-\frac{\psi_{N+1,j} - \psi_{N-1,j}}{2\Delta r} + \sum_{h=0}^{L-1} A_h^s F_{h,j}^s + \sum_{h=0}^{L-1} B_h^s G_{h,j}^s = 0$$

which come from the simplified interface of the displacement (equations (3.28) and (3.29)). The two blocks that follow that come from the simplified interface of the stresses (equations (3.30) and (3.31))

$$\frac{\phi_{N+1,j} + \phi_{N-1,j}}{\Delta r^2} - \sum_{h=0}^{L-1}\left(\frac{2}{\Delta r^2} + C_h^p\right) F_{h,j}^p - \sum_{h=0}^{L-1}\left(\frac{2}{\Delta r^2} + D_h^p\right) G_{h,j}^p = 0$$

$$\frac{\psi_{N+1,j} + \psi_{N-1,j}}{\Delta r^2} - \sum_{h=0}^{L-1}\left(\frac{2}{\Delta r^2} + C_h^s\right) F_{h,j}^s - \sum_{h=0}^{L-1}\left(\frac{2}{\Delta r^2} + D_h^s\right) G_{h,j}^s = 0.$$

Finally, come the recursion equations.

$$2lG^p_{lj} - (l-1)^2 F^p_{l-1,j} - \frac{F^p_{l-1,j+1} - 2F^p_{l-1,j} + F^p_{l-1,j-1}}{\Delta\theta^2} = 0 \tag{3.42}$$

$$2lF^p_{lj} + l^2 G^p_{l-1,j} + \frac{G^p_{l-1,j+1} - 2G^p_{l-1,j} + G^p_{l-1,j-1}}{\Delta\theta^2} = 0 \tag{3.43}$$

$$2lG^s_{lj} - (l-1)^2 F^s_{l-1,j} - \frac{F^s_{l-1,j+1} - 2F^s_{l-1,j} + F^s_{l-1,j-1}}{\Delta\theta^2} = 0 \tag{3.44}$$

$$2lF^s_{lj} + l^2 G^s_{l-1,j} + \frac{G^s_{l-1,j+1} - 2G^s_{l-1,j} + G^s_{l-1,j-1}}{\Delta\theta^2} = 0. \tag{3.45}$$

The previous equations can be combined into a matrix A that will used in the system $A\mathbf{U} = \mathbf{b}$. The resulting unknown vector for the system of equations is as follows

$$\begin{aligned}\mathbf{U} = \Big[&\overbrace{\phi_{0,1}\cdots\phi_{0,m}\ \psi_{0,1}\cdots\psi_{0,m}}^{\text{at ghost points}}\ \overbrace{\phi_{1,1}\cdots\psi_{1,m}}^{\text{at obstacle}}\ \overbrace{\phi_{2,1}\cdots\psi_{2,m}\cdots\phi_{N-1,1}\cdots\psi_{N-1,m}}^{\text{at interior grid points}}\ \overbrace{\phi_{N+1,1}\cdots\psi_{N+1,m}}^{\text{at ghost points}} \\ &\overbrace{F^p_{0,1}\ldots F^s_{0,m}\ G^p_{0,1}\ldots G^s_{0,m}\ldots\ F^p_{L-1,1}\ldots F^s_{L-1,m}\ G^p_{L-1,1}\ldots G^s_{L-1,m}}^{\text{at artificial boundary}}\Big]^T.\end{aligned} \tag{3.46}$$

Note the similarities to the setup of the acoustic system, seen in Equation 2.44. While the known vector **b**, for a soft obstacle boundary condition on the obstacle, is given by

$$\mathbf{b} = \Big[\overbrace{(OS)^1_1\ldots(OS)^1_m\ (OS)^2_1\ldots(OS)^2_m}^{\text{at ghost points}}\ \overbrace{0\ldots0\ldots0\ldots0}^{\text{at obstacle}}\ \overbrace{0\ldots0\ldots0\ldots0}^{\text{at all other points}} \Big]^T, \tag{3.47}$$

$$(OS)^1_j = \left[\lambda k_p^2 - 2\mu(ik_p\cos(\theta_j))^2\right](\phi_{inc})_{1,j}$$

$$(OS)^2_j = 2\mu(ik_p)^2\cos(\theta_j)\sin(\theta_j)(\phi_{inc})_{1,j}.$$

The known vector **b**, for a hard obstacle boundary condition on the obstacle, is given by

$$\mathbf{b} = \Big[\overbrace{(OH)^1_1\ldots(OH)^1_m\ (OH)^2_1\ldots(OH)^2_m}^{\text{at ghost points}}\ \overbrace{0\ldots0\ldots0\ldots0}^{\text{at obstacle}}\ \overbrace{0\ldots0\ldots0\ldots0}^{\text{at all other points}} \Big]^T, \tag{3.48}$$

$$(OH)^1_j = -ik_p\cos(\theta_j)(\phi_{inc})_{1,j}$$

$$(OH)^2_j = ik_p\sin(\theta_j)(\phi_{inc})_{1,j}.$$

3.5 NUMERICAL RESULTS

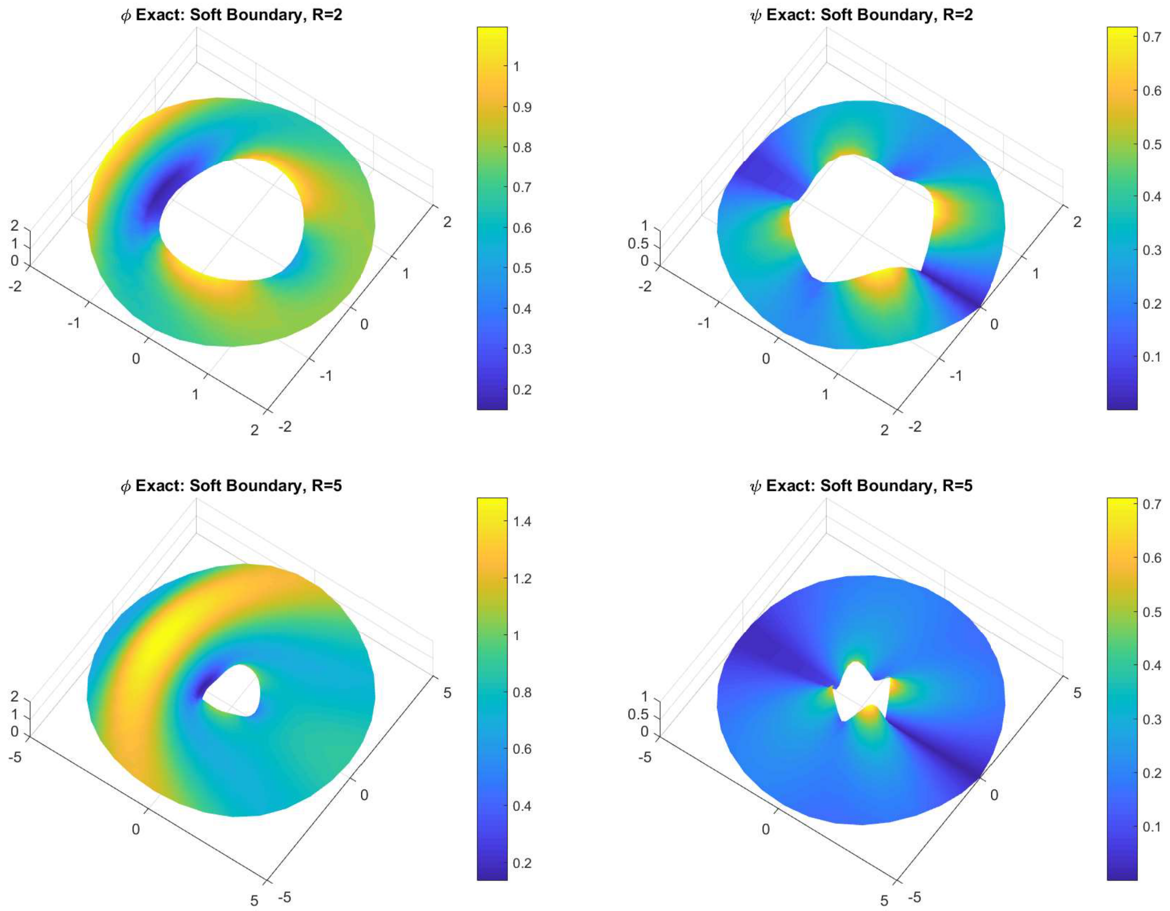

Figure 3.1: Example solutions for elastic wave scattering. On the left is ϕ and on the right ψ. All plots show solution for a soft obstacle boundary. Outer radius $R = 2$ for the top plots with $R = 5$ for the bottom plots. The data used is $r_0 = 1, \nu = .3, \rho = 1, E = 1$, NKFE$= 6$.

To analyze the accuracy and convergence of the proposed high order numerical method, I performed a set of experiments for the scattering of a time-harmonic incident elastic wave from a circular obstacle of radius r_0. The equations describing the incident wave are given in terms of the scalar potentials ϕ and ψ as

$$\phi(r_0, \theta) = \phi_{inc}(r_0, \theta) = e^{ikx} = e^{ikr\cos\theta}, \qquad \text{and} \quad \psi(r_0, \theta) = \psi_{inc}(r_0, \theta) = 0.$$

I performed experiments using various numbers of Karp expansion terms as well as various radii. Results for both hard and soft obstacle boundaries are included. Desired second order convergence

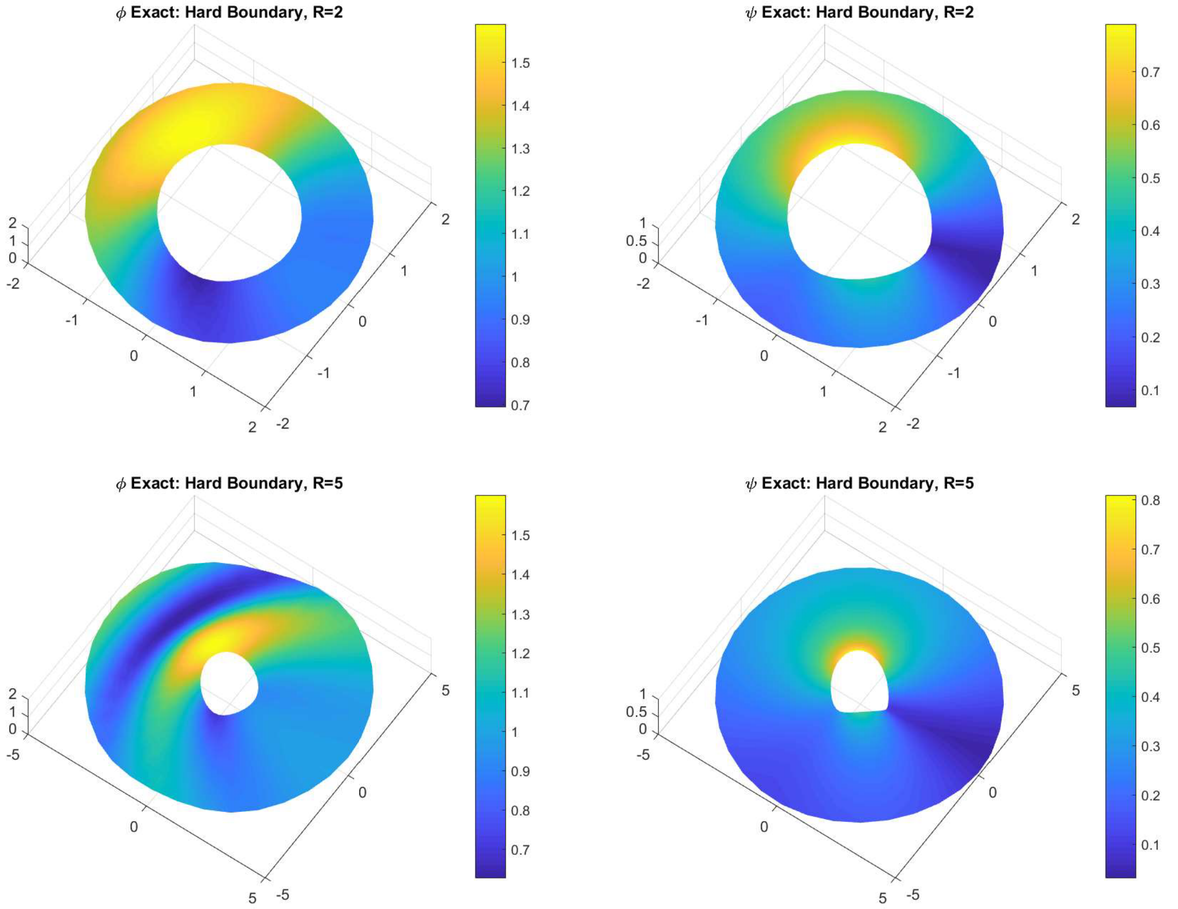

Figure 3.2: Example solutions for elastic wave scattering. On the left is ϕ and on the right ψ. All plots show solution for a hard obstacle boundary. Outer radius $R = 2$ for the top plots with $R = 5$ for the bottom plots. The data used is $r_0 = 1, \nu = .3, \rho = 1, E = 1$, NKFE$= 6$.

is demonstrated in various cases, confirming the second order nature of the scheme developed in the preceding section. As in the heterogeneous case, no exact solution was used so a series of increasingly refined grids was employed and the results over the most refined grid were taken as a reference (best approximation to the exact solution values) instead of the actual values of the exact solution.

Various examples of the reference solution of the total field for the two scalar wave potentials are shown in Figures 3.1 and 3.2. Both hard and soft obstacle boundary results are included, as well as several radii for the soft obstacle case. In Figure 3.3 order of convergence for the soft obstacle with outer radius 2 is shown. As can be seen in the figure, convergence of both potentials is consistent with a least squares logarithmic slope of 2 which matches the expected order of the scheme. More precise results, matching those in the figure, are shown for the scalar potentials ϕ and ψ in Tables 3.1 and 3.2, respectively. The values of $r_0 = 1$, $\nu = .3$, $\rho = 1$, $E = 1$ of the radius of the circular obstacle and elastic parameters are fixed during the experiments of this section. This gives $\lambda = \frac{E*\nu}{(1+\nu)(1-2\nu)} \approx .577$ and $\mu = \frac{E}{2(1+\nu)} \approx .385$. This in turns gives the wave numbers $k_p = \sqrt{\rho/(\lambda + 2\mu)} \approx .862$ and $k_s = \sqrt{\rho/\mu} \approx 1.613$ [28].

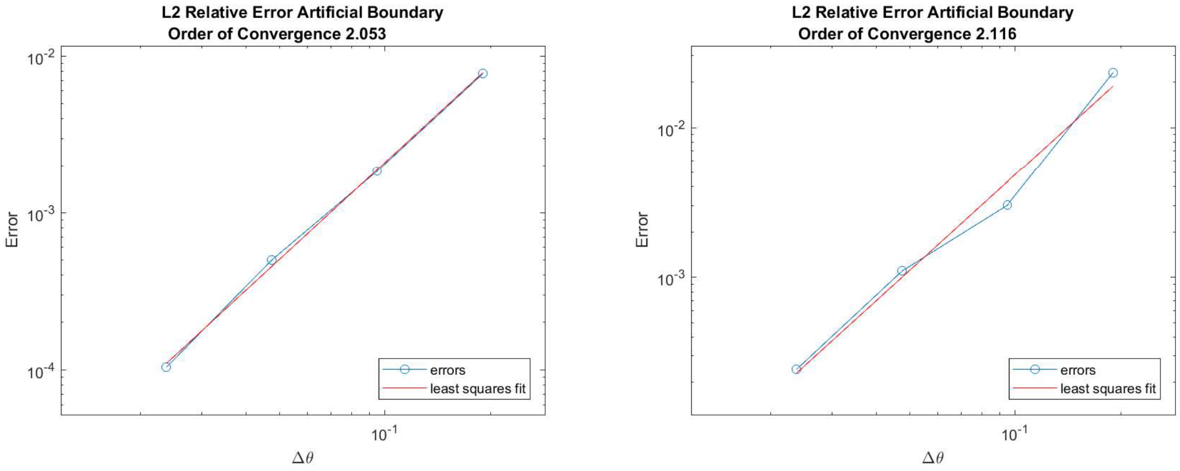

Figure 3.3: Line of best fit for order of convergence for the elastic scattering problem with soft obstacle boundary. Left plot shows convergence for ϕ and right plot shows ψ. Data comes from Tables 3.1 and 3.2.

$h = \Delta\theta = \Delta r$	L^2-norm Rel. Error	Observed order
0.1904	7.67×10^{-3}	
0.0952	1.84×10^{-3}	2.06
0.0476	4.98×10^{-3}	1.89
0.0238	1.03×10^{-4}	2.27

Table 3.1: Grid spacing, L^2 Relative Error, and order of convergence for elastic scattering problem with soft obstacle boundary. Results are shown for ϕ with R=2 and NKFE= 13.

$h = \Delta\theta = \Delta r$	L^2-norm Rel. Error	Observed order
0.1904	2.31×10^{-2}	
0.0952	3.01×10^{-3}	2.94
0.0476	1.10×10^{-3}	1.46
0.0238	2.43×10^{-4}	2.17

Table 3.2: Grid spacing, L^2 Relative Error, and order of convergence for elastic scattering problem with soft obstacle boundary. Results are shown for ψ with ϕ with R=2 and NKFE= 13.

$h = \Delta\theta = \Delta r$	L^2-norm Rel. Error	Observed order
0.3696	4.06×10^{-2}	
0.1848	7.39×10^{-3}	2.46
0.0924	1.85×10^{-3}	2.00
0.0462	3.85×10^{-4}	2.27

Table 3.3: Grid spacing, L^2 Relative Error, and order of convergence for elastic scattering problem with soft obstacle boundary. Results shown for ψ. Results shown for ϕ with R=4 and NKFE= 6.

These results are not surprising, because the interior scheme developed in the previous sections is only order 2. All finite difference approximations of derivatives were done up to second order so, although the Karp expansion is arbitrary order, the scheme is expected to reach 2nd order convergence. This is clearly seen in Figure 3.3 and Tables 3.1-3.3. Thus, my results confirm the consistency and accuracy of the finite difference scheme developed in this section.

Results similar to those found in Figure 3.3 were found by varying the number of Karp expansion terms from as low as 5 to as high as 19. When varying the outer radius R, similar results were also achieved as can be seen in Table 3.3. As a note, with larger radii, convergence was generally slightly more erratic but was always close to order 2. Results for the hard obstacle followed a similar pattern, if not slightly worse.

CHAPTER 4. CONCLUDING REMARKS AND FUTURE WORK

I have constructed an arbitrary high order numerical method for the two-dimensional time-harmonic acoustic scattering problem. This is based on applying a general pth order DC finite difference technique to approximate the Helmholtz equation (interior approximation) and the Karp's farfield expansion absorbing boundary condition (KFE-ABC). The number of terms, NKFE for the equations (2.8)-(2.12) defining the KFE-ABC needs to be adjusted to achieve the desired order of convergence.

The DC approximation of the governing Helmholtz equation of arbitrary order p is given by (2.30), while the pth order DC approximation of the Karp's farfield expansion ABC with enough

NKFE terms is given by the discrete equations (2.33)-(2.34), (2.35)-(2.36). The algebraic linear system for the scattered field obtained from all these discretizations is completed by the discrete equations corresponding to the continuity of the scattered field (2.8) at the artificial boundary and the appropriate discretization of the boundary condition at the obstacle (2.7). In the case of Neumann or Robin condition, a pth order DC finite difference discretization of the boundary condition at the obstacle should be constructed. The details in the construction of this DC scheme for the BVP (2.6)-(2.12) are given in Section 2.3.

It is seen from Figs. 2.3 - 2.5 and Figs. 2.7 - 2.8 that the proposed method can reach its theoretical order of convergence, if enough terms in Karp's expansion are retained for sufficiently fine grids. This fact confirms the arbitrary high order character of the KFE-ABC that was claimed in [17]. Actually, this high order property was already observed in [30] where the KFE-ABC was combined with a high order isogeometric finite element method employed as a Helmholtz solver for the interior.

The virtue of this approach is that any pth order approximation of the Helmholtz equation consists of the same 5-point stencil which is used by the standard centered second order finite difference approximation. The difference between these two approximations is that the right hand side of the pth order scheme includes some additional terms that come from leading terms of the truncation error of the Helmholtz equation centered second order finite difference approximation. These new terms are calculated from a $(p-2)$th order numerical solution $\mathbf{U^{p-2}}$, previously computed. Hence, the proposed DC method is an iterative technique. For instance, the application of the DC fourth order method that leads to a fourth order approximation $\mathbf{U^4}$ is preceded by the calculation of $\mathbf{U^2}$ by applying a second order DC scheme. Moreover, the matrix defining the LSE associated to both steps is the same matrix A_2. However, it is important to notice (as shown in Fig. 2.2) that this matrix, although highly sparse, is not banded due to the presence of the unknown angular functions of the Karp's expansion. In Section 2.5, I describe this iterative process in detail.

In Section 2.3, I rigorously proved how my proposed DC finite difference method is consistent with equations (2.6)-(2.12), defining the KFE-BVP, to any order p. In Section 2.6, these theoretical results are complemented experimentally by showing that the numerical solutions obtained by applying KDC4 and KDC6 numerically converge to the exact solution with a fourth and sixth order convergence rate, respectively.

I accessed the computational effectiveness of my proposed technique by choosing target tolerance errors to be satisfied by the numerical FFP. An analysis of the right plot in Fig. 2.6 reveals that KDC4 reaches the tolerance errors faster than its standard counterpart KS4. This is remarkable since the combined KDC4 technique requires the solution of two linear systems while KS4 needs to solve only one linear system. I attribute this performance to the greater sparsity of KDC4 matrix A_2 compared with the less sparse matrix A_4, associated to the 9-point standard finite difference approximation of Helmholtz equation. I also notice that KS4 requires more KFE terms than KDC4 for similar grid sizes to reach a given tolerance error. But, more important KDC6 is eight times faster than KDC4, although its application has one more step in the iterative process. The reason for this is the coarser grid and lower number of KFE terms used by KDC6 compared with those employed by KDC4. For instance, KDC6 reaches an error close to 10^{-5} for (PPW,NKFE) = (26,7), while KDC4 needs (PPW,NKFE) = (60,8).

In addition to developing a scheme for the homogeneous case, I also extended the deferred corrections method to the heterogeneous case using (2.54). For media with continuous changes in the index of refraction, such as (2.58), it was shown that a deferred corrections scheme could obtain up to 6th order convergence (see Figure 2.10). For media with discontinuous changes in the index of refraction, such as (2.59), the convergence results were not quite as robust. Overall, the extension to the heterogeneous case was successful.

After developing the deferred corrections scheme for the acoustic case, I moved on to the construction and analysis of numerical methods for elastic wave scattering problems. First, the original Navier's equation of elasticity was reduced to two uncoupled Helmholtz equations for the scalar potentials ϕ and ψ. This was done by decomposing the elastic displacement in terms of these two scalar potentials. Then, I constructed a high order ABC based on Karp's infinite series representations of the scalar elastic potentials ϕ and ψ in the farfield which resulted in the

KFE-ABC given by (3.13)-(3.20). Finally, the Helmholtz equations for the two scalar potentials were complemented with the KFE-ABC and the boundary condition over the obstacle boundary to finalize the definition of the KFE-BVP.

Numerical methods for the scattering of elastic waves of two different types of obstacles were discussed. Numerical results confirmed the second order convergence of this method.

In this work, I chose to limit my study to the two-dimensional Helmholtz equation in polar coordinates for clarity in the formulation and presentation of the theoretical results. However, I anticipate that an extension of the DC technique to the KFE-BVP in generalized curvilinear coordinates will follow a similar pattern to what has already been observed in polar coordinates. This extension could be based on Villamizar and Acosta's previous works on the grid generation for single and multiple scatterers of complexly shaped geometries [31, 32]. These grids correspond to generalized curvilinear coordinates conforming to the boundaries of the scatterers. Moreover, these grids were used by the same authors to solve single and multiple scattering problems from complexly shaped obstacles in [33, 34, 17]. In particular in [17], they obtained second order convergence for a star shaped scatter with smooth boundary by using second order finite difference approximation based on curvilinear coordinantes conforming to the scatterer boundary.

Another possible extension is moving to the three-dimensional Helmholtz equation in spherical coordinates

$$\Delta_{r,\theta,\phi}u + k^2u = u_{rr} + \frac{2}{r}u_r + \frac{1}{r^2\sin\theta}(\sin\theta\ u_\theta)_\theta + \frac{1}{r^2\sin^2\theta}u_{\phi\phi} + k^2u = 0, \tag{4.1}$$

coupled with the high order local farfield expansion ABC for the three-dimensional case (WFE), which was constructed in [17] from the Wilcox's farfield expansion. In addition, it is expected that the KFE can be adapted to wave problems in the half-plane with a hard or soft condition on the plane boundary. A technique similar to the procedure employed by Acosta and Villamizar in [34] for the construction of the Dirichlet to Neumann (DtN) condition for a single obstacle in the half-plane from the multiple DtN condition for the full-plane [35, 33] is expected to be used. It is also my opinion that the extension of the DC method to arbitrary PDEs (as long as the solution is sufficiently regular) is possible. The theoretical foundation for such an extension would be found in the proof of Theorem 2.6.

APPENDIX A. SIXTH ORDER DC FINITE DIFFERENCE APPROXIMATIONS

The sixth order DC finite difference approximation to the Helmholtz differential operator is obtained by substituting $p = 6$ in (2.30) which leads to

$$\begin{aligned}\mathcal{H}^6 U^6_{ij} \equiv \mathcal{H}^2 U^6_{ij} &- \left(\frac{1}{3! r_i} D^4_{3r} U^4_{ij} + \frac{2}{4!} D^4_{4r} U^4_{ij} + \frac{2}{4! r_i^2} D^4_{4\theta} U^4_{ij} \right) h^2 \\ &- \left(\frac{1}{5! r_i} D^2_{5r} U^4_{ij} + \frac{2}{6!} D^2_{6r} U^4_{ij} + \frac{2}{6! r_i^2} D^2_{6\theta} U^4_{ij} \right) h^4, \qquad \text{(A.1)}\end{aligned}$$

where $D^4_{4r} U^4_{ij}$, $D^4_{3r} U^4_{ij}$, and $D^4_{4\theta} U^4_{ij}$ are fourth order approximations of $(u_{4r})_{ij}$, $(u_{3r})_{ij}$, and $(u_{4\theta})_{ij}$, respectively. They are obtained by applying standard centered fourth order finite difference to U^4_{ij} and are given by

$$(u_{4r})_{ij} \approx D^4_{4r} U^4_{ij} \equiv \frac{1}{\Delta r^4} \left[\frac{-1}{6} U^4_{i-3,j} + 2 U^4_{i-2,j} - \frac{13}{2} U^4_{i-1,j} + \frac{28}{3} U^4_{i,j} - \frac{13}{2} U^4_{i+1,j} + 2 U^4_{i+2,j} - \frac{1}{6} U^4_{i+3,j} \right] \qquad \text{(A.2)}$$

$$(u_{3r})_{ij} \approx D^4_{3r} U^4_{ij} \equiv \frac{1}{\Delta r^3} \left[\frac{1}{8} U^4_{i-3,j} - U^4_{i-2,j} + \frac{13}{8} U^4_{i-1,j} - \frac{13}{8} U^4_{i+1,j} + U^4_{i+2,j} - \frac{1}{8} U^4_{i+3,j} \right] \qquad \text{(A.3)}$$

$$(u_{4\theta})_{ij} \approx D^4_{4\theta} U^4_{ij} \equiv \frac{1}{\Delta \theta^4} \left[\frac{-1}{6} U^4_{i,j-3} + 2 U^4_{i,j-2} - \frac{13}{2} U^4_{i,j-1} + \frac{28}{3} U^4_{i,j} - \frac{13}{2} U^4_{i,j+1} + 2 U^4_{i,j+2} - \frac{1}{6} U^4_{i,j+3} \right]. \qquad \text{(A.4)}$$

Also, $D^2_{6r} U^4_{ij}$, $D^2_{5r} U^4_{ij}$, and $D^2_{6\theta} U^4_{ij}$ are second order approximations of $(u_{6r})_{ij}$, $(u_{5r})_{ij}$, and $(u_{6\theta})_{ij}$, respectively. They are obtained by applying standard centered second order finite difference to U^4_{ij} and are given by

$$(u_{5r})_{ij} \approx D^2_{5r} U^4_{ij} \equiv \frac{1}{\Delta r^5} \left[\frac{-1}{2} U^4_{i-3,j} + 2U^4_{i-2,j} - \frac{5}{2} U^4_{i-1,j} + \frac{5}{2} U^4_{i+1,j} - 2U^4_{i+2,j} + \frac{1}{2} U^4_{i+3,j} \right] \tag{A.5}$$

$$(u_{6r})_{ij} \approx D^2_{6r} U^4_{ij} \equiv \frac{1}{\Delta r^6} \left[U^4_{i-3,j} - 6U^4_{i-2,j} + 15U^4_{i-1,j} - 20U^4_{i,j} + 15U^4_{i+1,j} - 6U^4_{i+2,j} + U^4_{i+3,j} \right] \tag{A.6}$$

$$(u_{6\theta})_{ij} \approx D^2_{6\theta} U^4_{ij} \equiv \frac{1}{\Delta \theta^6} \left[U^4_{i,j-3} - 6U^4_{i,j-2} + 15U^4_{i,j-1} - 20U^4_{i,j} + 15U^4_{i,j+1} - 6U^4_{i,j+2} + U^4_{i,j+3}. \right] \tag{A.7}$$

For points close to the artificial boundary, appropriate one-sided finite difference approximations are employed.

APPENDIX B. APPROXIMATIONS FOR THE NEUMANN BOUNDARY CONDITION

In the case of the Neumann condition at the boundary of a circular obstacle of radius r_0, the strategy to be employed for the construction of the fourth order approximation follows very closely the one employed at the artificial boundary for the KFE in subsection 2.3.2.

First, I consider the standard second order centered finite difference approximation for the Neumann boundary condition at $r = r_0$, retaining an approximation of its leading order truncation error,

$$\frac{U^4_{2,j} - U^4_{0,j}}{2\Delta r} = -\frac{\partial u_{\text{inc}}}{\partial r} + \frac{\Delta r^2}{6} (Dr)^2_{3r} \, U^2_{1,j}. \tag{B.1}$$

This equation contains the ghost values $U^4_{0,j}$. They are also present in the fourth order approximation of the Helmholtz equation (2.19) evaluated at $i = 1$. Therefore, they can be eliminated by combining these equations. The equations (B.1) and (2.19) also contain second order approximations of one-sided third and fourth forward radial derivatives at $r = r_0$, respectively. They act on the second order approximations $U^2_{1,j}$ of u obtained in the first step and they are given by

$$(Dr)^2_{3r}\, U^2_{1,j} \equiv \frac{1}{\Delta r^3}\left[-\frac{3}{2}U^2_{0,j} + 5U^2_{1,j} - 6U^2_{2,j} + 3U^2_{3,j} - \frac{1}{2}U^2_{4,j}\right], \tag{B.2}$$

$$(Dr)^2_{4r}\, U^2_{1,j} \equiv \frac{1}{\Delta r^4}\left[2U^2_{0,j} - 9U^2_{1,j} + 16U^2_{2,j} - 14U^2_{3,j} + 6U^2_{4,j} - U^2_{5,j}\right]. \tag{B.3}$$

It can be shown that the DC formula (B.1) is also a fourth order approximation to the Neumann boundary condition and its proof is completely analogous to those performed in Section 2.3. Therefore, it is not included.

I can increase the fourth order discrete approximation (B.1) of the Neumann condition to an arbitrary pth order. Again, the definition is a natural extension of (B.1), where the continuous derivatives of higher order truncation error terms $(u_{3r})_{1j}$, $(u_{5r})_{1j}, \ldots, \left(u_{(p-1)r}\right)_{1j}$ are approximated by appropriate right one-sided discrete operators acting on the previously calculated $(p-2)$th ordered numerical solution $U^{p-2}_{i,j}$, approximating the exact solution u. More precisely,

$$\frac{U_{2,j} - U_{0,j}}{2\Delta r} = -\frac{\partial u_{\text{inc}}}{\partial r} + \frac{h^2}{3!}(Dr)^{p-2}_{3r}U^{p-2}_{ij} + \frac{h^4}{5!}(Dr)^{p-4}_{5r}U^{p-2}_{ij} + \ldots + \frac{h^{p-2}}{(p-1)!}(Dr)^2_{(p-1)r}U^{p-2}_{ij}. \tag{B.4}$$

The proofs that the finite difference formulas (2.33)-(2.36) and (B.4) approximate their continuous counterparts to pth order are very similar to the proof of Theorem 2.6. Therefore, they are omitted. The key assumption for these proofs is that the discrete functions $U^{p-2}_{N,j}$, $F^{p-2}_{l-1,j}$ and $G^{p-2}_{l-1,j}$, which are obtained in a previous step, are $(p-2)$th order approximations of the continuous solutions $u(R,\theta)$, $F^2_{l-1}(\theta)$, and $G^2_{l-1}(\theta)$, respectively.

BIBLIOGRAPHY

[1] A Bayliss, C.I Goldstein, and E Turkel. On accuracy conditions for the numerical computation of waves. *Journal of Computational Physics*, 59(3):396 – 404, 1985.

[2] Arnaud Deraemaeker, Ivo Babuška, and Philippe Bouillard. Dispersion and pollution of the fem solution for the helmholtz equation in one, two and three dimensions. *International Journal for Numerical Methods in Engineering*, 46:471 – 499, 08 1999.

[3] I. Babuska and S. Sauter. Is the pollution effect of the fem avoidable for the helmholtz equation considering high wave numbers? *SIAM J. Numer. Anal.*, 34(6):2087–2502, 1997.

[4] K. Wang and Y. S. Wong. Polution-free finite difference scheme for non-homogeneous helmholtz equation. *Int. J. Numer. Anal. Mod.*, 11(4):787–815, 2014.

[5] I Singer and E Turkel. High-order finite difference methods for the helmholtz equation. *Comput. Methods Appl. Mech. Eng.*, 163(1-4):343–358, 1998.

[6] I Singer and E. Turkel. Sixth-order accurate finite difference schemes for the helmholtz equation. *J. Comput. Acoust.*, 14(3):339–351, 2006.

[7] G. Sutmann. Compact finite difference schemes of sixth order for the helmholtz equation. *J. Comput. Appl. Math.*, 203(1):15–31, 2007.

[8] M. Nabavi, K. Siddiqui, and J. Dargahi. A new 9-point sixth order accurate compact finite-difference method for the helmhotz equation. *J. Sound Vib.*, 307:972–982, 2007.

[9] L. Collatz. *The numerical treatment of differential equations*. Springer-Verlag, 1960.

[10] R.J. LeVeque. *Finite Difference Methods for Ordinary and Partial Differential Equations*. SIAM, Philadelphia, 2007.

[11] Y. Zhang, K. Wang, and R. Guo. Sixth-order finite difference scheme for the Helmholtz equation with inhomogeneous robin boundary condition. *Add. Diff. Equ.*, 362:1–15, 2019.

[12] A. Bayliss, M. Gunzburger, and E. Turkel. Boundary conditions for the numerical solution of elliptic equations in exterior regions. *SIAM J. Appl. Math.*, 42:430–451, 1982.

[13] B. Engquist and A. Majda. Absorbing boundary conditions for the numerical simulation of waves. *Math. Comput.*, 31:629–651, 1977.

[14] K. Feng. Finite element method and natural boundary reduction. In F. Magoulès, editor, *Proc. of the International Congress of Mathematicians*, pages 207–232, 1983.

[15] Y. Li and Z. J. Cendes. Modal expansion absorbing boundary conditions for two-dimensional electromagnetic scattering. *IEEE Transactions on Magnetics 29*, 29(2):1835–1838, 1993.

[16] D. Givoli. High-order local non-reflecting boundary conditions : a review. *Wave Motion*, 39:319–326, 2004.

[17] V. Villamizar, S. Acosta, and B. Dastrup. High order local absorbing boundary conditions for acoustic waves in terms of farfield expansions. *J. Comput. Phys.*, 333:331–351, 2017.

[18] S Britt, S Tsynkov, and E Turkel. A compact fourth order scheme for the helmholtz equation in polar coordinates. *J. Sci. Comput.*, 45:26–47, 2010.

[19] M. Medvinsky, S. Tsynkov, and E. Turkel. High order numerical simulation of the transmission and scattering of waves using the method of difference potentials. *J. Comp. Phys.*, 243:305–322, 2013.

[20] M. Medvinsky, S. Tsynkov, and E. Turkel. Solving the helmholtz equation for general smooth geometry. *Wave Motion*, 62:75–97, 2016.

[21] V. Pereyra. Iterated deferred corrections for nonlinear boundary value problems. *Numer. Math.*, 11:111–125, 1968.

[22] V. Pereyra. Highly accurate numerical solution of quasilinear elliptic boundary-value problems. *Math. Comp.*, 24:771–783, 1970.

[23] S. N. Karp. A convergent “farfield expansion” for a two-dimensional radiation functions. *Comm. Pure Appl. Math.*, 14:427–434, 1961.

[24] T. Hagstrom and S. Hariharan. A formulation of asymptotic and exact boundary conditions using local operators. *Appl. Num. Math.*, 27:403–416, 1998.

[25] P. Martin. *Multiple Scattering*. Cambridge Univ. Press, 2006.

[26] O. P. Bruno and E. M. Hyde. Higher-order fourier approximation in scattering by two-dimensional, inhomogeneous media. *SIAM J. Numer. Anal.*, 42:2298–2319, 2005.

[27] P. Chadwick and E. A. Trowbridge. Elastic wave fields generated by scalar wave functions. *Pro. Camb. Phil. Soc.*, 63:1177–1187, 1967.

[28] Yih-Hsing Pao and Mow Chao-Chow. *Diffraction of Elastic Waves and Dynamic Stress Concentrations*. The Rand Corporation, 52 Vanderbilt Avenue New York, New York 10017, 1973.

[29] Dan Givoli and Joseph B. Keller. Non-reflecting boundary conditions for elastic waves. *Wave Motion*, 12(3):261 – 279, 1990.

[30] T. Khajah and V. Villamizar. Highly accurate acoustic scattering: Isogeometric analysis coupled with local high order farfield expansion ABC. *Comput. Methods Appl. Mech. Engrg.*, 349:477–498, 2019.

[31] V. Villamizar and S. Acosta. Elliptic grids with nearly uniform cell area and line spacing. *Electron. Trans. Numer. Anal.*, 34:59–75, 2009.

[32] V. Villamizar and S. Acosta. Generation of smooth grids with line control for scattering from multiple obstacles. *Math. Comput. Simul.*, 79:2506–2520, 2009.

[33] S. Acosta and V. Villamizar. Coupling of Dirichlet-to-Neumann boundary condition and finite difference methods in curvilinear coordinates for multiple scattering. *J. Comput. Phys.*, 229:5498–5517, 2010.

[34] S. Acosta, V. Villamizar, and B. Malone. The DtN nonreflecting boundary condition for multiple scattering problems in the half-plane. *Comput. Methods Appl. Mech. Engrg.*, 217-220:1–11, 2012.

[35] M. Grote and C. Kirsch. Dirichlet-to-Neumann boundary conditions for multiple scattering problems. *J. Comput. Phys.*, 201:630–650, 2004.